Influence of Channel Bend Curvature on Debris-Flow-Driven Avulsion on Alluvial Fans, Explored through Discrete Simulations

By

Jonathan Teboul

May, 2023

Director of Thesis: Scott Lecce, PhD

Major Department: Department of Geography, Planning, and Environment

Alluvial fan morphology is often influenced by channelization of fluvial flow and episodic instances of avulsion (channel rerouting). Under certain conditions and in response to dramatic shifts (i.e., significant vegetation loss) or significant weather activity (i.e., intense rainfall or snowmelt) in the upstream environment, debris flows can manifest and have devastating impacts on downstream environments and communities. During their transport downstream through meandering distributary channels, debris flows can incise into the channel bed and laterally into channel banks. Debris flows can also rise and overtop the banks of their confining channels. These overtopping events are especially prevalent along channel bends where increases in centrifugal forces influence manifestations in debris-flow superelevation. This study investigates the parameter of channel bend curvature for debris-flow-driven avulsion using a debris-flow flume housed in the ECU Geomorphic Modeling Laboratory and series of 3D-printed rectangular channels of differing sinuosity imprinted in a simulated alluvial plain. The results of this experiment suggest variability in channel curvature (sinuosity) influences variability in manifestations of debris-flow runout and inundation behaviors, including debris-flow avulsion location, volumes and distances of debris-flow runout, and channel bend and alluvial plain

inundation. Specifically, greater volumes and surface area coverages of debris-flow runout are suggested to result from avulsions from sharper curves as opposed to wider curves. Zones of likelihood of inundation that incorporate these findings are presented for areas of intersect between debris flows and channel outer bend crests on the debris-flow flume. Sharper curves are also suggested to influence greater frequency of avulsion. Lastly, this study demonstrates the potential for debris-flow avulsions to occur in channels free of debris pileup and as direct results of flow superelevation.

INFLUENCE OF CHANNEL BEND CURVATURE ON DEBRIS-FLOW-DRIVEN AVULSION ON ALLUVIAL FANS, EXPLORED THROUGH DISCRETE SIMULATIONS

A Thesis

Presented to the Faculty of the Department of Geography, Planning, and Environment

East Carolina University

In Partial Fulfillment of the Requirements for the Degree

Master of Science in Geography

by

Jonathan Teboul

May, 2023

Director of Thesis: Scott Lecce, PhD
Thesis Committee Members:
Thad Wasklewicz, PhD
Hannah Sirianni, PhD

© Jonathan Teboul, 2023

Acknowledgments

I would like to acknowledge the wealth of support I have received from family, friends, and mentors during my experience at ECU toward the completion of my thesis. Thank you, Dr. Thad Wasklewicz, Dr. Scott Lecce, and Dr. Hannah Sirianni, for the opportunity to merge my passions for geomorphology, geohazards, and remote sensing and conduct great research under your combined mentorship. Thank you, Mr. Rob Howard, for your support and expertise in all things technical. Thank you to my friends Michael Trapani and Maximilian Martinez- Michael for the support and help in designing parts for the debris-flow flume, and Maximilian for the support and extensive help in the lab. Thank you to my brother Eric Teboul for the endless support and assistance in all things academic but mostly statistics. Finally, thank you ECU Water Resources Center for awarding me the title of Water Scholar and funding to complete my research.

TABLE OF CONTENTS

LIST OF TABLES

LIST OF FIGURES

INTRODUCTION

Background

Debris-flow-driven avulsions can occur and are episodic, and potentially devastating events along rivers and channelized alluvial fans. Superelevation, channel plugging, or a lack of channel capacity can cause debris to leave the channel to produce a new flow pathway (Whipple and Dunne, 1992; de Haas et al., 2019; Densmore et al., 2019). Debris-flow runout (the debris-flow in its depositional state) and other flows navigating newly specified flow paths then pose serious risks to human life and infrastructure on the fan or adjacent to a stream channel. Society is also currently unequipped to predict debris-flow runout trajectories rapidly and reliably (Kean et al., 2019). Therefore, a need exists to further advance the scientific understanding of the parameters that influence debris-flow runout trajectories, especially after avulsions.

Research into the parameters suspected of initiating debris-flow-driven avulsions on alluvial fans has been evolving rapidly. Such avulsions are primarily thought to be caused by one of several mechanisms. One mechanism includes progressive backstepping in debris-flow deposition (Schumm et al., 1987; Suwa et al., 2009; Okano et al., 2012; de Haas et al., 2016). Similarly, avulsions may also be influenced by the deposition of exceptionally large particles in the channel, introducing instability and warranting flow pattern adjustment (Leenman and Eaton, 2021). Avulsions may also occur due to the overflow of the mainstem banks of the alluvial fan, particularly at sharp outer bends close to the fan apex (Procter, 2012; de Haas et al., 2018; Zubrycky et al., 2021).

This experiment was designed to expand knowledge of debris-flow-driven avulsion behavior on channelized alluvial fans. This study evaluates the role of channel bend curvature on

debris-flow runout volumes and areas of inundation following evacuations from simulated debris-flow channels.

Debris-flow initiation and dynamics

Debris flows initiate with little warning and manifest as saturated mixtures of sediment and other materials entrained by runoff after intense rainfall. Their velocities (2 – 10 m/s (Suwa et al., 1993; Galgaro et al., 2005; Turnbull et al., 2015)) and volumes are often destructive in the context of infrastructure and dwellings. Channels bounded by steep slopes in mountainous areas are known to be prominent sources of initiation for debris flows (Davies, 1990; Scheidl et al., 2014; Wang et al., 2020). Debris flows are frequently generated in first-order channels. Lower-order tributaries generally comprise the steepest portions of the drainage network (Martin, 2007; Prancevic et al., 2014; Florsheim and Chin, 2021), and contain poorly consolidated alluvial/colluvial beds. The alluvial/colluvial deposits are a primary source of sediment for debris flows (Huang and Tang, 2014). Debris-flow initiation following rapid channel bed mobilization has been suggested to occur where channel slopes exceed approximately 22° (Prancevic et al., 2014). Debris flows may also be initiated by other processes such as channel bank failure (Ellet et al., 2019), stormwater flow over knickpoints and impact with colluvium below, generating failure (Griffiths et al., 2004; Parise and Cannon, 2012; Florsheim and Chin, 2021), or following wildfires and associated loss of vegetation (Gabet, 2003; Florsheim and Chin, 2021) and other organic (i.e., fungal) life (Mardhiah et al., 2016). Following initiation, debris flows can build up their volume in a snowball-effect fashion where the clearing of steep tributary channels such as small headwater gullies contributes varying concentrations of loose unconsolidated sediment to the active debris-flow mass (Kean et al., 2013; Florsheim and Chin, 2021). As the debris-flow

reaches shallower slopes with wider accommodation space (generally upon entry to an alluvial fan), it gradually loses kinetic energy, and this negative feedback mechanism leads to sediment deposition often in a fan-shaped feature.

Wildfires and the resulting loss of organic life can enhance conditions conducive to debris flows. Vegetation and organic matter near the surface form a canopy that protects soil, sediments, and bedrock from erosion caused by rainsplash and Hortonian overland flow. Additionally, root structures and mycelia (Mardhiah et al., 2016) help to anchor the sediment in the underlying soils, as noted by Florsheim and Chin (2021). Florsheim and Chin (2021) further state that vegetation can also provide a means for trapping and storing loose sediment derived from upslope, thus making these sediments susceptible to failure following wildfires. Wildfires can contribute to erosion by removing natural anchors in the soil, and by creating a hydrophobic layer in soils (thus increasing runoff), which sometimes produces a plane of weakness in the soil (Florsheim and Chin, 2021) for future thin debris flows following the burial of the hydrophobic surface (Gabet, 2003). Therefore, the combined effects of wildfires and loss of biotic functions and structures lead to erosion, thus providing ready sources of unconsolidated sediment for debris flows.

Debris-flow avulsions

Debris flows can travel unchannelized in alluvial settings (de Haas, 2016) and be deposited on debris-flow fans that evolve as sequences of debris-flow pileups and intermittent avulsions (channel abandonment, and subsequent creation elsewhere) (de Haas et al., 2016; de Haas et al., 2018). De Haas et al. (2018) describe this process as when debris flows are deposited atop one another in an upslope, aggradational fashion, decreasing the slope of the general

depositional area until an avulsion can incise a channel through the buildup. The avulsion steepens the slope and allows runout access to the rest of the radial length of the fan.

Debris flows can also travel as channelized flows. Debris-flow-driven avulsions (henceforth referred to as debris-flow avulsions in this paper) in channelized settings have been observed to occur from debris-flow overspilling/overtopping of fluvial channel banks during their descent down alluvial fans. Overtopping is expected along channel bends, where increases in centrifugal forces induce increases in gradients of flow superelevation and thus greater likelihoods of spillage (Procter, 2012; Scheidl et al., 2014; Zubrycky et al., 2021) and bank failure (Nieto at al., 2022). Scheidl et al. (2014) report larger superelevation angles with increases in grain size along channels with constant bend radii. Numerous authors (e.g., Nichols, 1991; de Haas et al., 2018; Leenman and Eaton, 2021) further suggest bank overspilling by debris flows often occur when flows of large enough size are assisted by previous channel plugging events. Where de Haas et al. (2018) argue channel plugging reduces channel capacity, Leenman and Eaton (2021) argue these plugs may also play a role in flow diversion and prompting flow pattern adjustment.

Debris-flow inundation

Humans have historically settled in mountainous valley regions to take advantage of conditions favorable to agriculture (Bull, 1977; Boyer et al., 2006; Cavalli and Marchi, 2008) (Figure 1). Generally, alluvial fans at the outlets of these valleys can host fertile soils and conveniently accessible supplies of water (Boyer et al., 2006). The gradual down-fan loss of flow energy causes deposition of coarser-grained materials near the fan head and finer grains in the distal fan region (Bahrami and Ghahraman, 2019). As a result of this sorting regime, coarser-

grained deposits make fan head regions act as recharge zones with deeper groundwater tables, and finer-grained deposits of lower permeability along the distal ends of fans store the descending groundwater in shallow-depth aquifers (Skaggs and de Ridder, 1996).

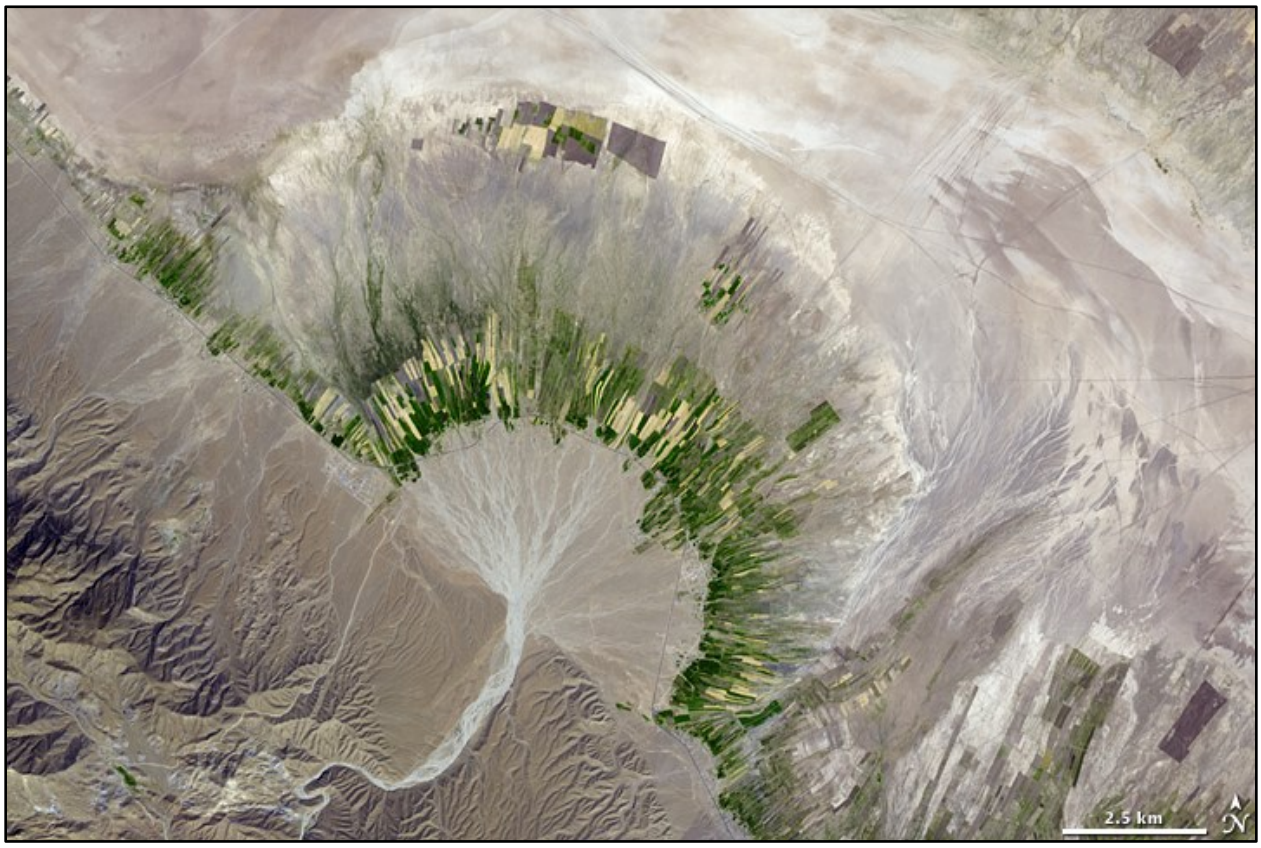

Figure 1. Satellite image of agriculture spread along the periphery of the base of an alluvial fan fed by an ephemeral stream. Zagros Mountains, southern Iran (Allen, 2008).

However, the allure of environmental conditions essential to agriculture also comes with its hazards to inhabitants and infrastructure on and adjacent to the alluvial fan. Debris-flows mark the presence of an active landscape subject to change, and change can happen rapidly and dramatically as with the destruction of large swaths of infrastructure and loss of life. A debris-flow can occupy the full radial width of a fan even in channelized settings (Davies, 2008), and thus there is the potential for areas downstream to be inundated by debris flows that may far exceed the width of their original channels as demonstrated by Kean et al. (2019). These authors

provide an inundation map for San Ysidro Creek following the 9 January 2018 Montecito debris-flow event in California, where debris flows had in certain places inundated areas more than 10x wider than the established FEMA 100-year floodplain. Such concerns are rarely discussed among individuals involved in the development of properties on fans; developers are especially prone to build simply upon approval from local municipalities and consider hazards once all payments have been collected (Davies, 2008). Sometimes these municipalities also fail to account for the full threats of danger from debris flows in their own regulations, such as in the removal of debris flows as a qualified hazard from the Building Act of 2004 in New Zealand (McSaveney, 2005). The abilities of most mountain communities to properly react to these hazards are further minimized by their very common denial of access to participate in economic and political activities (Huang et al., 2020).

Physical modeling experiments

Geomorphologists use physical models to study the mechanisms of creation and natural evolution of landforms. Models are used to simulate the processes of landscape formation under wide ranges of environmental conditions from within controlled settings. Many fundamental observations regarding alluvial fan shape and processes were derived from small-scale experiments conducted by Roger LeB. Hooke, William L. Rohrer, and Stanley A. Schumm in the latter half of the 20th century (Adams, 2017). These observations were also sometimes validated with in-field observations as a way of defining similarity of process (Hooke, 1967) assuming lab and field-based measurements are not influenced by scale, as stated by Paola et al. (2009).

However, as simplifications of macro-scale dynamics, physical models often generalize the myriad parameters potentially involved in the creation of the natural processes being studied,

adding substantial limitation to the accuracies of results. For instance, models that assess debris-flow transport in alluvial settings may disregard instances of channelized transport. Numerous previous attempts have been made to model debris-flow behavior using flumes (e.g., Iverson, 1997; Iverson et al., 2010; Procter, 2012; Scheidl et al., 2014; de Haas, 2016; Adams, 2017), however, the flume-based flows from these experiments mostly deposited sediment on unchannelized outflow plains following their descent down steep chutes. Where debris-flow transport behaviors through simulated fluvial channels were indeed assessed, instances of overspilling were often not foci of study (e.g., Scheidl et al., 2014) or were specifically prevented (e.g., Procter, 2012).

Objective

This experiment uses a physical modeling approach wherein 3D data are derived from a model simulating debris-flow avulsion. The flume and sediment mixture used in this experiment were designed based on specifications from de Haas (2016) and validated later in research by Adams (2017) and Adams et al., (2019). However, where de Haas (2016) and later Adams (2017) focused on non-confined flows in simulated outflow plains, this experiment focuses on confined (channelized) flow in the simulated outflow plain. The simulations are designed in a way to further constrain the behaviors of debris-flow runout and inundation under varying channel curvatures.

Research questions

1) Can debris-flow avulsions be modeled in channels free of clogs/prior debris?

2) Are there common zones of avulsion according to sine curvature?
3) Is there a correlation between channel sinuosity and the occurrence of avulsion and debris-flow runout phenomena in simulated alluvial fan environments?

METHODS

Description of the physical model

The flume (Figure 2) consists of a sediment-agitation tank that releases saturated sediment mixtures (simulating debris flows) into a feeder channel/chute that conveys material downslope onto an outflow plain (a simulated alluvial plain). The sediment agitation tank is a partially-manually operated cylindrical device 0.5 m x 0.3 m in dimension. A remotely operated hatch installed at the exit of the tank allows sediment slurries access to the flume chute. The hatch is opened via a series of pneumatic hoses that run from an air compressor seated behind the flume. The flume chute measures 2 m long by ~0.15 m wide by ~0.15 m tall, lined along its base with 80 grit sandpaper to simulate natural slip surface roughness, and is raised at a 30° angle to the outflow plain (Adams, 2017). A hatch is installed midway down the chute to modulate the amount of water entering the outflow plain and reduce disturbances of channel morphology by the incidental flow of excess water (Adams, 2017). The chute hatch measures ~0.08 m long by ~0.18 m wide and is opened 1.5 seconds following debris-flow release from the agitation tank, as the bulk of flow sediments reach the outflow plain before this time. The outflow plain is a square box with a 10° dip measuring 2 m x 2 m with ~0.11 m of elevated borders, filled 0.06 m high with an unconsolidated reference mixture free of clay and water (Adams, 2017). A manually operated scraper is installed atop the outflow plain to level the sediment bed back to a 6 cm height after each experimental trial run.

Figure 2. Photo of the debris-flow modeling flume situated in the ECU Geomorphic Modeling Laboratory.

Selection of channel curvatures

Before conducting the physical modeling experiment, precise measurements of sinuosity (K) were necessary to determine the appropriate channel morphologies to use. Sinuosity is a dimensionless measurement representing the length of a channel between two chosen endpoints divided by the straight-line distance traversed between said endpoints. Determination of arc length within channel bends, however, can be difficult; it can be done simplistically yet imprecisely by taking the sum of a small series of chosen straight-line distances along a bend or

by using integration. These measurements can be done more precisely (following the same concept of taking the sum of a series of straight-line segments, but to infinitesimally small degrees) using integration (Eq. 1.1; Eq. 1.2; Eq. 2) if the equation of the curve follows the general format of $y = f(x)$ and the function (f) is continuously differentiable (LibreTexts, 2020) (true for the sine functions used in this experiment and thus appropriate for the purpose of deriving measurements for sinuosity).

Each straight-line segment is given by the equation for distance between two points on a Euclidian plane, as follows:

$$D = \sqrt{(x_2 - x_1)^2 + (y_2 - y_1)^2} \qquad (1.1)$$

or

$$D = \sqrt{(dx)^2 + (dy)^2} \qquad (1.2)$$

where *D* is distance, x is the starting point, and y is the endpoint (adapted from LibreTexts, 2020). When applied to the integration approach, the equation becomes:

$$L = \int_a^b \sqrt{1 + \left(\frac{dy}{dx}\right)^2}\, dx \quad \text{if } y = f(x), a \leq x \leq b \qquad (2)$$

where *L* is arc length, and *a* and *b* are endpoints from $x = a$ to $x = b$ (adapted from LibreTexts, 2020). This approach was used for the preparation of four model channels, where arc lengths of each channel divided by their corresponding straight-line distances to derive sinuosity.

A series of four channel curves were chosen to represent a wide range of situations between the upper and lower extremes of channel sinuosity ($1.0 < K < 2.5+$ according to Leeder, 1973, and $1.05 < K < 2.76+$ for ephemeral meandering streams according to Billi et al., 2018).

Billi et al. (2018) states values where K ≈ 1 define virtually straight channels, and values of 2.5 < K < 2.76 define highly sinuous channels (Billi et al., 2018). The initial three curves chosen early in the experiment follow sinusoidal paths representing ideal meandering channel morphology (Langbein and Leopold, 1966; Leeder, 1973; Williams, 1986), and are related by the repeated doubling in magnitude of frequencies from the periods 1π to 4π. A fourth curve created later in the experiment was chosen as an intermediary curve to capture avulsions between the sin(1x) and sin(2x) curves. The first channel (Channel 1) follows the equation $y = \sin(2x)$. This channel is represented by a period of 1π m and K of 1.68, inspired by Leeder (1973) who suggested that a sinuosity of 1.7 represents an optimal midpoint value between straight (K = 1.0) and very sinuous (K = 2.5) rivers. A K of 1.7 is an approximate representation of "mixed-load streams of intermediate sinuosity" (Leeder, 1973, p. 268, citing Schumm (1972)). Channel 2 follows the equation $y = \sin(1x)$. This channel is represented by a period of 2π m and a K of 1.22, representing both double the wavelength of Channel 1 and a visually reasonable approximation of sinuosity for an alluvial channel of 10° inclination. This approximation is supported by the Rosgen Stream Classification System (Rosgen, 1994) when applied to Type-A streams, which suggests such streams on a 10° slope will have a sinuosity of < 1.2 ± 0.2 units. Channel 3 follows the equation $y = \sin(0.5x)$. This channel is represented by a period of 4π m and a K of 1.06, representing both double the wavelength of Channel 2 and a nearly straight channel by Billi et al.'s (2018) standards. Channel 4 follows the equation sin(1.5x). This channel is represented by a period of 4π/3 and a K of 1.43.

Modeling of channel curvatures

Sine functions for the series of four model channels were first visualized in 2D using the online Desmos Graphing Calculator interface. Next, the series of channels were visualized in 3D using Blender, assigning *XYZ Math Surface* meshes that plotted according to set X, Y, and Z axes. The X, Y, and Z axes are defined by functions of "u" and "v". The X-axis was assigned the equation $y = f(u)$; the Y-axis was assigned the equation $y = f(v)$; and the Z-Axis was assigned the equations $y = f(\sin(2v))$ for Channel 1, $y = f(\sin(v))$ for Channel 2, $y = f(\sin(0.5v))$ for Channel 3, and $y = f(\sin(1.5v))$ for Channel 4. Parameters *U Min*, *U Max*, *U Step*, *U Wrap*, *V Min*, *V Max*, and *V Step* were also specified: *U Min* was left at the default value of 0, where *U Max* (channel height) was assigned a value of 0.127 m (12.7 cm, or roughly the maximum depth of the outflow plain from sandpaper base to the top of each elevated border). *U Step* (the number of subdivision surfaces) was raised from its default value of 32 subdivisions to 200 subdivisions to increase the number of mesh faces, thereby smoothening the mesh surface. *V Min* was left at the default value of 0, where *V Max* (channel length) was set to π m (3.14 m), 2π m (6.28 m), 4π m (12.56 m), and 4π/3 m (4.19 m), for Channel 1, Channel 2, Channel 3, and Channel 4, inclusive.

Modeled channels were scaled according to the channel width vs. depth ratio as proposed by Williams (1986). This author states that regardless of sinuosity, bankfull width (W) = $21.3D^{1.45}$ if bankfull mean depth (D) falls between 0.03 m and 18 m (his equation 38). The flume chute width of 0.15 m limits the maximum possible channel width to 0.15 m and channel depth to ~0.034 m, and the channels were thus modeled in Blender to reflect these dimensions.

The four channels produced in Blender were trimmed to ≤ ½ wavelength to only render best representatives of initial wave crests (the first bends in the channel), which was also done to

accommodate the limited size of the 2 m x 2m outflow plain area. Channels were then sliced widthwise at roughly 0.10 – 0.15 m intervals using Autodesk Fusion 360 for fabrication via 3D printing.

When finished, the printed channels adopt rectangular profiles along their bases, ideal for preparing channels impacted by debris-flow scour (Ellet et al., 2019). To create imprints of these models in the sediment lining the outflow plain, the general profiles of the models are first carved out of the sediment with a small shovel. Second, the channels are lowered into the sediment approximately 0.06 m deep. Third, the channels are buried along their sides, dampened with water from a low-pressure hose, and carefully lifted out of the outflow plain. Lastly, approximately 0.01 m (1 cm) of sand is placed along the channel bed to bring the channel depth close to 0.05 m (5 cm). While the channel depth was intended to lie at 0.034 m (3.4 cm), the choice to only re-bury the channel 1.0 cm deep was made to limit the amount of sediment able to be scoured off the channel bed and deposited in the runout zone. Lowering the overall alluvial bed height to compensate for this issue was not conducted at this time.

The orientations at which each printed channel was imprinted into the alluvial plain differed from their natural expected angles. In the experiment, the channels were rotated clockwise. The sin(2x) channel was rotated 60°, the sin(1.5x) channel was rotated 55°, the sin(1x) channel was rotated 40°, and the sin(0.5x) channel was rotated 30° (Figure 3). Naturally, debris-flow channels are generally aligned such that their meanders will rarely buckle back upslope. However, the sin(1.5x) and sin(2x) channels would eventually climb back upslope if either curve were extrapolated to complete full sine wave cycles. For a 10° slope, such an occurrence would be unlikely in nature. Clockwise channel rotations were performed to allow debris-flow masses conveyed down chute immediate access to straight-line lengths of the

channels. Cutting the channels such that the debris flows would immediately encounter a bend would require removal of half of the bend crest, otherwise the chute and each channel would intersect in an oblique fashion. It was necessary to keep as much of the curves as possible by cutting each channel at their respective sine wave inflection points and allowing flows access to the straight-line channel lengths to focus debris-flow trajectories on the channel crests.

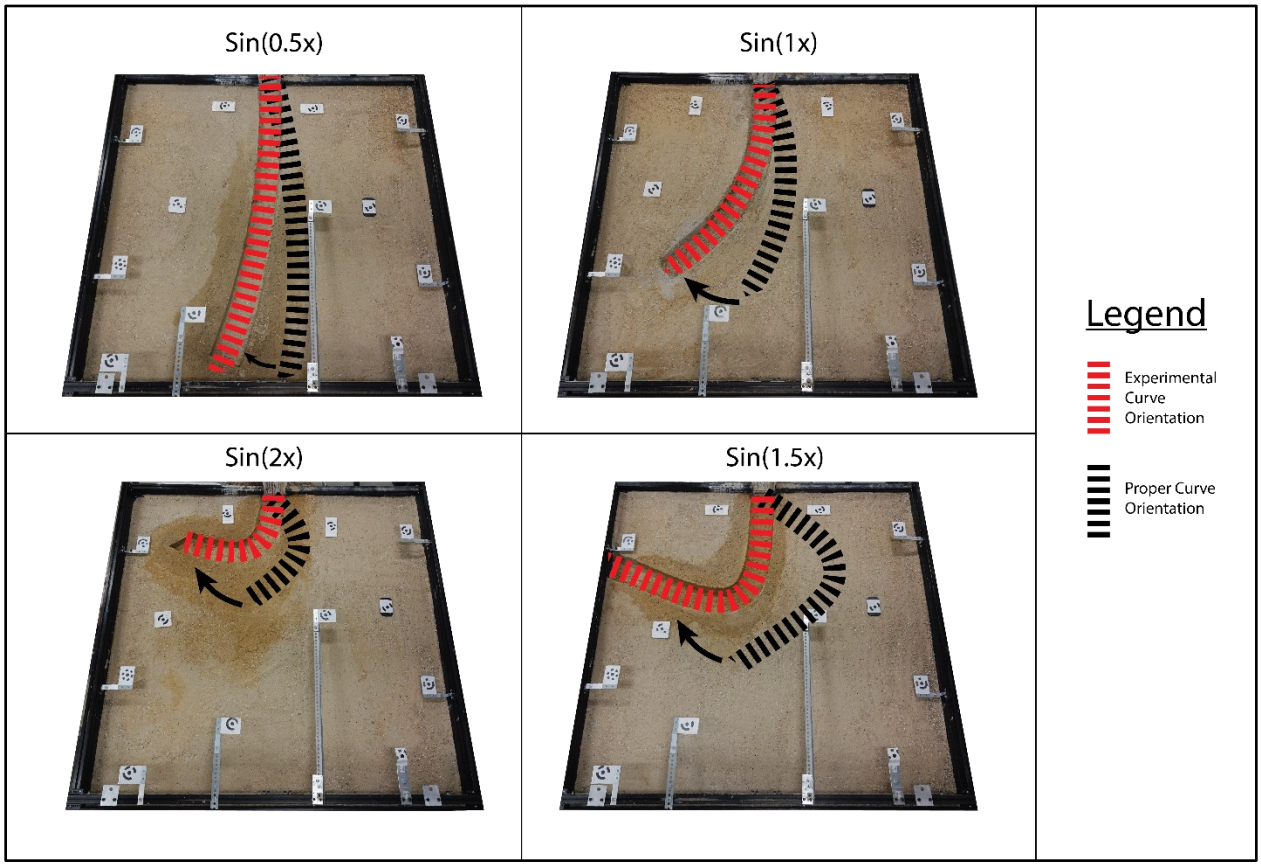

Figure 3. Visualization of rotation per experimental channel. Experimental curve orientation represents the orientation used in the experiment. Proper curve orientation represents expected downslope channel orientation.

Photographic techniques

In deviation from the original setup as approached by Adams (2017), the debris-flow modeling apparatus was retrofitted with a constellation of 20 Sony RX0 II cameras in lieu of the

Leica P40 Terrestrial Laser Scanner (TLS) used to collect photographic data in previous experiments (Adams 2017). This change from a 3D-scanning solution provided by the TLS to a solely two-dimensional one provided by the Sony camera array represents the switch from using LiDAR to photogrammetry for 3D modeling purposes. Nonetheless, the combined camera geometry and quantity in the new setup interestingly result in higher spatial resolution and similar (if not slightly better) accuracy to those provided by the TLS.

Debris-flow composition

The composition of each debris-flow mixture remained fixed throughout the experiment (Table 1). This composition was established in de Haas (2016) and used previously in experiments by Adams (2017). The debris-flow mixture composition was based on comparison to a reference composition collected by de Haas (2016).

Table 1. Experimental debris-flow composition adapted from Adams (2017) and de Haas (2016).

Baseline Debris-Flow Composition						
Units	Gravel	Coarse Sand	Fine Sand	Clay	Water	Total Mass
Grams	865	2837	1010	288	1650	6650
Wt.%	13.01	42.65	15.18	4.34	24.82	100
Vol.%	17.31	56.73	20.19	5.77	0.47	100

Trials

Prior to each trial, the laboratory was prepared to enhance trial efficiency. Steps taken to enhance efficiency included confirming there was enough reference mixture and raw components to prepare the debris-flow masses; confirming cameras were operational, seated

firmly, and had clear lenses; maintaining optimal pressure in the air compressor; confirming the lab computer was ready to receive images; confirming the debris-flow mixing tank was empty; cleaning the flume chute of debris; clearing previous debris-flow masses from the alluvial plain; rebuilding the channel in the alluvial plain using the sand leveler, a shovel, and the 3D printed channel inserts alongside sparse amounts of water; burying the channel to a 5 cm depth using reference mixture; and mixing the sedimentary components of the experimental debris-flow masses in a bucket according to proper specifications (Figure 4).

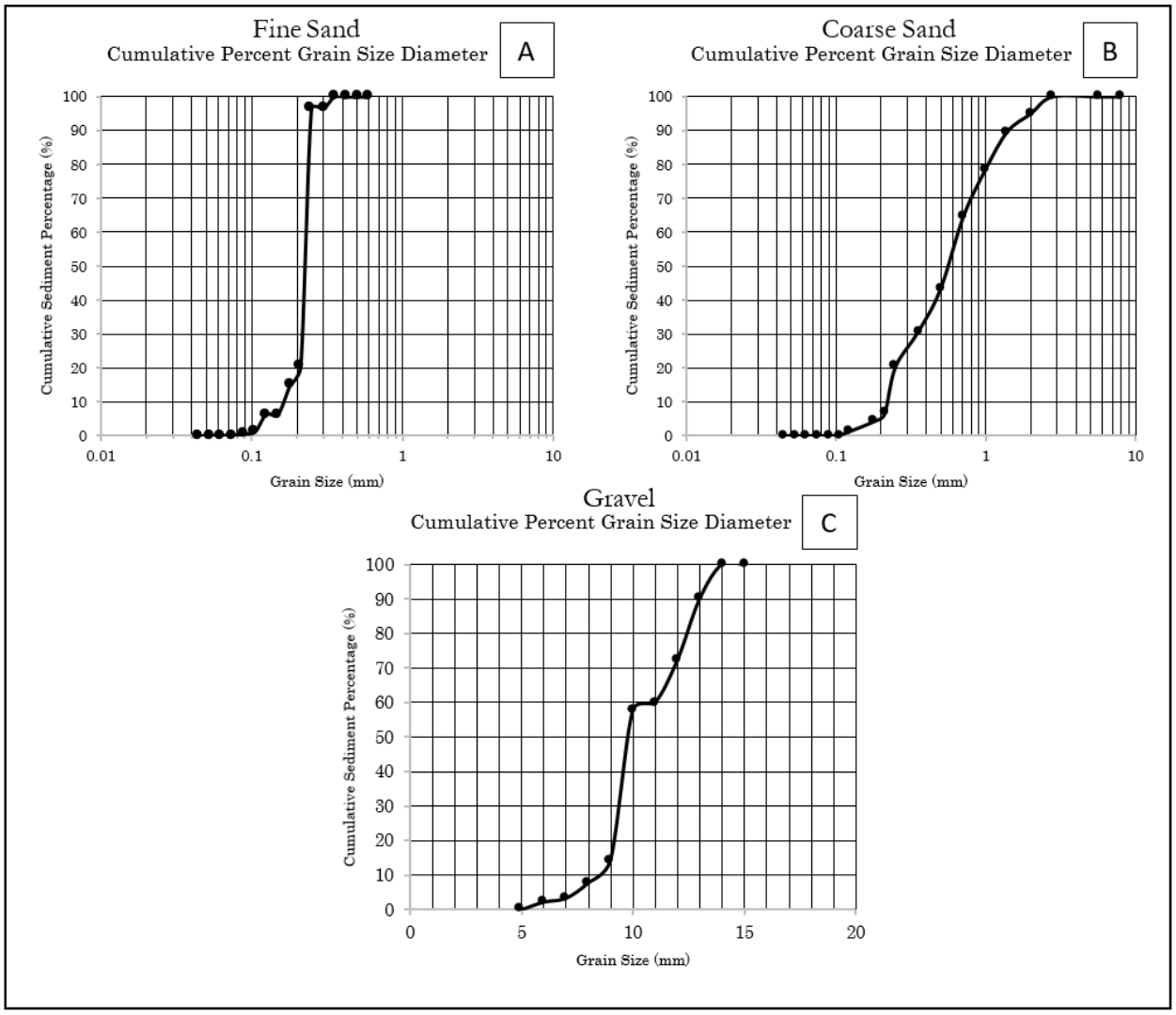

Figure 4. Grain size distribution of A) fine sand, B) coarse sand, and C) gravel constituents composing each simulated debris-flow mixture.

Trials were performed in a consistent manner, and included the following steps: prompting the DSLR camera to begin recording; combining the bucket of sediment with 1,650 grams of water and immediately pouring the mixture into the flume mixing tank; mixing the materials rigorously for roughly 10 seconds; opening the mixing tank hatch by connecting the pneumatic hoses running from the air compressor; waiting for the chute hatch to automatically open 1.5 seconds after debris-flow release; waiting roughly 10 seconds for the bulk of the debris-flow mass to settle in the outflow plain; taking a snapshot of the outflow plain from the entire camera array simultaneously; and ending the DSLR recording.

A total of 30 trial runs, plus two to three extra runs, were performed per sine curve, where each trial consisted of one 'baseline' scan and one 'after' scan. The extra runs were collected in anticipation of possible errors only to be found during processing. Trials without significant error were considered successful, and those with significant error were removed from post-processing in the experiment. Significant error included > 1.0 cm of photo alignment error and those resulting from camera focus issues, improper Ground Control Point (GCP) placement, and debris-flow flume malfunctions such as stuck hatches and broken equipment.

Control point positioning

A set of twelve circular 12-bit GCPs were positioned throughout the outflow plain at varied elevations (from the maximum height of the outflow plain frame down to the alluvial bed) and in locations not anticipated to interfere with predicted debris-flow runout paths. The GCPs had originally been positioned in a static fashion, though during the experiment had been accidentally displaced in various manners. The GCPs worked as reference points to consistently align photographs collected between runs into a common coordinate system.

Developing a Cartesian Coordinate system

A cartesian coordinate system was developed for the outflow plain using a Leica P40 TLS in conjunction with the program Leica Cyclone Register 360 upon termination of the last trial run of the experiment. The TLS was used to scan the debris-flow simulation environment after the final trial of the sin(1.5x) set of trials, and Cyclone Register 360 was used to extract XYZ coordinates for each GCP in the outflow plain. These coordinates were used as reference points to align the models during later processing in Agisoft Metashape.

Processing photogrammetry data

Photo alignment was performed in Agisoft Metashape using key point limits of 75,000 and tie point limits of 4,000 when processing each scan, as these limits were default values preselected by the program. Brief trial by error otherwise showed imperceptible change in alignment error with reduction to 60,000 key points (the maximum recommended limit when working with high quality imagery in Metashape as suggested by Over et al. (2021)) and increase to 5,000 tie points as previously used in established geomorphological literature (Cooper et al., 2021). Camera alignment optimization was performed immediately after, using Metashape's default camera parameters alongside adaptive camera model fitting and estimates of tie point covariance.

Issues such as image noise, improper GCP placement, and poor focus during photography can produce outliers when generating depth measurements for point clouds, warranting correction for such outliers in post-processing. GCPs responsible for alignment errors exceeding

1.0 cm were discarded from the analysis to reduce total alignment error; these GCPs included numbers 11, 17, and 43 for all trials in the sin(1x) group, and numbers 11, 17, 31, 40, 43, and 140 in the sin(2x) group (see Figure 5 for GCP arrangement). Throughout the experiment, the number of GCPs was consistently maintained above the absolute minimum of 3 GCPs required for georeferencing, with a total of 12 initial GCPs and no reduction below the minimum threshold at any point.

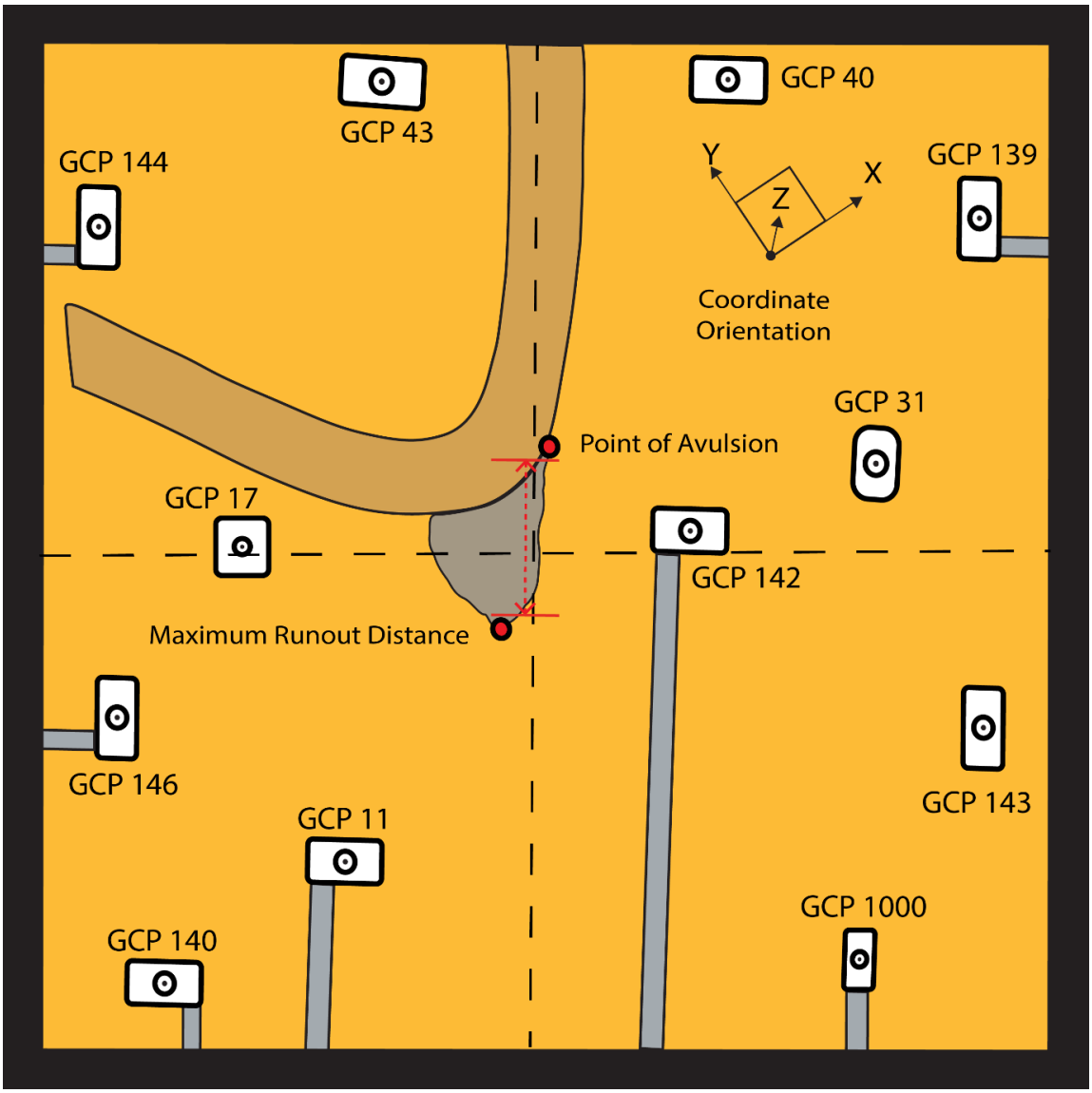

Figure 5. Illustration of method for determining debris-flow runout maximum distance on the alluvial bed.

Poor focus during photography was a concern when using the Sony RX0 II cameras comprising the debris-flow flume camera array. These cameras use the rolling shutter image capture method, which can be a limitation in photogrammetric reconstruction (Cooper et al., 2021). However, this was mitigated by keeping the cameras in static positions and only generating models for the outflow plain when in fully settled states.

Dense point clouds were built in Agisoft Metashape at high quality with aggressive depth filtering. These point clouds were produced using structure-from-motion - multiview stereo (SFM-MVS) techniques. SFM-MVS is a photogrammetric process by which 2D image stereopairs collected from various perspectives and overlapping at least 60% can be meshed to create bifocal views of objects, thus permitting 3D/depth analyses (Andries, 2005). Dense clouds where avulsions were not observed, or where avulsions occurred, but a total alignment errors exceeding 1.0 cm was produced, were discarded from the analysis.

Digital Elevation Models (DEMs) were produced in Metashape immediately following the production of the dense clouds, using the dense clouds as the source data and inverse distance weighting interpolation (IDW) to account for unmeasured sections. IDW is a process wherein the value of an unmeasured region is estimated with respect to the values of its neighboring regions, and closer values attribute greater influence than distant regions. IDW is the default mechanism for the patching of unmeasured sections in dense clouds in Agisoft Metashape.

Debris-flow runout and profile inundation spatial statistics

At this point in the experiment, it had become apparent that avulsions were either unlikely to occur, or had only occurred once, between the sin(1x) and sin(0.5x) groups.

Therefore, these channels were not considered for tests of correlation and difference for the rest of the study. However, sin(1x) trial data are still reported and were used to help determine outflow bed alignment errors and probability of avulsion.

DEMs produced in Metashape were imported into ESRI ArcGIS Pro and clipped to their shared outflow plain boundary. DEMs of difference (henceforth referred to as DoDs in this paper) were prepared using the *difference* function in ArcGIS (Wheaton et al., 2009). Shapefiles were prepared to mark the horizontal boundaries of each observed avulsion runout region on the DoDs, and these runout regions were clipped to the extents of their shapefile traces. Zonal statistics were generated in ArcGIS wherein the area of each cell/pixel in the trace region was multiplied by their respective height values, and the sum of the products constituted the volume of each instance of debris-flow runout. This was done by first taking the sum of the height values for each cell/pixel in the DoD avulsion regions, deriving 'sum rasters' defined by one value – the sum – for each avulsion in the experiment. Second, the absolute value of the sum rasters was multiplied by the total two-dimensional areas of each DoD avulsion runout region (represented as *cell size (x)* multiplied by *cell size (y)* per region) to derive volume.

Several more metrics to represent the behavior of the debris-flow runouts were prepared. These included maximum runout distance, probability of avulsion, points of avulsion (uppermost segments of outer bend profile inundation), ranges of inundation of outer bend profiles (avulsion ranges), and zones of probability of inundation for the outer-bend profiles and the surface of the outflow plain. Maximum runout distance was calculated by using the distance formula between XYZ coordinates of avulsion to farthest downslope XYZ coordinates of runout along a constant linear (180° downslope) axis (Figure 5). Coordinates of avulsion were estimated from video recordings taken with the tripod-mounted Sony Alpha 7 III DSLR camera and more precisely

pinpointed in Agisoft Metashape, whereas coordinates of farthest downslope points of deposition were directly observed in Agisoft Metashape. Probability of avulsion was defined as the total number of avulsions observed over the total number of successful trials per sine curve. Zones of probability of inundation by outer-bend profile were calculated by utilizing the *Count Overlapping Features* tool in ArcGIS Pro for all runout traces between the sin(1.5x) and sin(2x) curves to find hotspots in inundation. A similar process was used for determining the probability of inundation by zone on either outer-bend profile, however, given these profiles were linear features, they were divided into near-equal segments (Figure 6) where each segment represented roughly 1% of the overall profile. Zones of probability of inundation were represented as regions where runout traces intersected the outer bend profiles with some recurring frequency.

Figure 6. Example of segmentation and labeling of sin(2x) curve outer bend.

Parametric unpaired t-tests with Welch's correction were performed to determine presence of statistically significant difference in avulsion location and outer bend profile segment inundation range (avulsion range) between sin(1.5x) and sin(2x). Determinations of statistically significant difference among sine curves would help elucidate possible significance of either sine curve as attempted earlier with the debris-flow runout statistics. Statistically insignificant results would otherwise indicate sine curvature likely did not play a role in influencing debris-flow behavior.

In anticipation of comparison with debris-flow runout data, tests of Gaussian distribution within the outer bend profile inundation and points of avulsion datasets were generated. Validation of Gaussian distribution enables the proper computation of Pearson correlation coefficients as opposed to nonparametric Spearman correlation coefficients during comparison with debris-flow runout datasets. Positive correlation between outer bend profile inundation and runout behaviors would suggest sine curvature has an impact on debris-flow runout behaviors in the simulated alluvial plain.

Data pertaining to maximum runout distance and runout volume per trial run were compiled in Microsoft Excel and exported into GraphPad Prism 9.5. This program was used to generate descriptive statistics, correlations, and similarity data resulting from t-tests. Descriptive statistics were prepared for volumes and maximum runout distances observed between sin(1.5x) and sin(2x). Pearson correlations accompanied with simple linear regressions were conducted to assess relationships between runout distances vs. volumes per channel. Following positive determination of Gaussian distributions inherent to the data, parametric unpaired t-tests with Welch's correction (implying unequal standard deviations within the dataset) were performed with chosen confidence intervals of 95%. These tests helped elaborate the existence of patterns in volumes vs. maximum runout distances between sin(1.5x) and sin(2x).

Data pertaining to outer bend profile inundation were compiled in Microsoft Excel. This program was used to generate measurements of mean, median, range, and standard deviation. These data were then exported to GraphPad Prism 9.5, where parametric unpaired t-tests with Welch's correction were prepared to discern relationships between magnitudes of outer bend profile inundation (avulsion ranges measured by count of intersected segments) vs. debris-flow volumes and maximum runout distances per channel with 95% confidence. Also, points of

avulsion were compared to debris-flow volumes and maximum runout distances. Similarly, tests of Gaussian distribution (D'Agostino & Pearson tests; Anderson-Darling tests; and Shapiro-Wilk tests) were also performed to confirm normality among the datasets. Measurements taken for spatial distribution of outer bend profile inundation and points of avulsion did not incorporate information for segment inundation range error on a per-trial basis.

Identification of error

Alignment error

Estimates of alignment error resulting from improper or inconsistent GCP placement were generated alongside supplemental visualizations of total GCP displacement throughout the experiment. These errors can produce offsets in dense point clouds prior to final DEM production. Errors in this sense typically manifest as lateral translation between DEMs when imported into ArcGIS, which can also skew measurements taken for runout and inundation behaviors.

Outflow plain position

Error in XYZ space between outflow plain coordinates observed during the experiment was logged. These assessments were made for a random assortment of trial runs, capturing the final outflow plain configurations following ‘after’ flows. Taking estimates of error between outflow plain coordinates helps estimate how accurately the outflow plain was leveled between each run, however, in this experiment were mainly taken to elaborate Z (elevation) errors produced between scans. While X and Y coordinates corresponding with each Z value were

taken, these are displayed solely for the purpose of demonstrating rough consistency in positions of measurement (within roughly 2 cm) for each coordinate where a Z value was observed. Accurate determination of Z error was necessary to establish elevation inaccuracies between DEMs imported into ArcGIS Pro where only X and Y values were known.

Outer bend profile inundation error

Determination of degree of error of outer bend profile inundation was a multifaceted process and was necessary to account for the variability in size inherent to all segments from either profile. Bins were considered inundated if they had any degree of interaction with the flows; this means the lateral degree of interaction could be over- or under-estimated by as much as +/- 2 bins of error, plus the associated bin size error. Calculating bin size error requires consideration of a specific study range, or the range of total segments inundated with debris. The generalized formula for estimating the total error of outer bend profile inundation follows the formula ((total inundated segments + 2 segments) * maximum bin size among segments) – ((total inundated segments – 2 segments) * minimum bin size among segments). These estimations were produced assuming the extra two segments maintain the greatest observed lengths among their respective profiles.

Order effect

Given the number of trials in the experiment, concerns were warranted over whether the methods for preparing and running each trial remained consistent or gradually shifted over time, which could influence results. Therefore, determinations of whether the order in which the trials

were conducted influenced trial outcome (a concept known as order effect) were assisted with Pearson correlations. These tests were performed on the sin(1.5x) group for run # vs. maximum debris-flow runout distance; debris-flow volume; outer bend profile inundation range; and points of avulsion. Similarly, these tests were performed on the sin(2x) group for run # vs. maximum debris-flow runout distance; debris-flow volume; outer bend profile inundation range; and points of avulsion.

RESULTS

Background

Each successful trial run was characterized by one rapid short-lived pulse that delivered unconsolidated sediment to the outflow plain. During trials where avulsions were observed, flow fronts appeared to be the first masses to evacuate the channel as shown by video recordings. Each avulsion in the experiment first initiated at a precise point (see: Table 2, Points of Avulsion) along the channel outer bend then widened to inundate broader portions of the outer bend profile before overtopping following flow superelevation.

Table 2. Debris-flow runout spatial statistics.

Sin1x										
Run #	Max Runout Distance (cm)	Pixel Area (cm^2)	Zonal Stats (SUM) (cm)	Volume (cm^3)	Point of avulsion			Farthest Downslope Point		
					X	Y	Z	X	Y	Z
22	27.976	0.009	-744.96	6.369	-1.320	1.003	-0.795	-1.103	0.836	-0.851
Sin1.5x										
Run #	Max Runout Distance (cm)	Pixel Area (cm^2)	Zonal Stats (SUM) (cm)	Volume (cm^3)	Point of avulsion			Farthest Downslope Point		
					X	Y	Z	X	Y	Z
3	16.992	0.008	-2137.48	17.952	-1.330	0.992	-0.793	-1.197	0.891	-0.825
4	49.267	0.009	-50065.14	428.294	-1.345	1.020	-0.789	-0.967	0.717	-0.875
5	25.273	0.008	5932.70	50.214	-1.350	1.023	-0.791	-1.150	0.875	-0.835
7	31.603	0.009	32376.13	278.126	-1.324	0.986	-0.798	-1.078	0.795	-0.850
8	26.114	0.008	16747.65	142.289	-1.340	1.010	-0.794	-1.136	0.853	-0.837
9	34.039	0.009	26211.35	223.786	-1.347	1.021	-0.792	-1.080	0.816	-0.847
10	24.049	0.008	22069.59	187.136	-1.306	0.949	-0.805	-1.120	0.800	-0.842
11	23.871	0.009	3521.70	29.965	-1.353	1.030	-0.789	-1.168	0.885	-0.829
12	27.178	0.009	26706.09	228.130	-1.315	0.973	-0.798	-1.103	0.809	-0.844
14	27.003	0.009	17655.62	150.208	-1.322	0.982	-0.797	-1.108	0.822	-0.842
15	16.537	0.008	5424.93	46.104	-1.305	0.963	-0.800	-1.178	0.861	-0.828
17	21.696	0.009	2989.52	25.623	-1.367	1.039	-0.778	-1.200	0.908	-0.820

18	21.651	0.009	2908.37	24.904	-1.353	1.019	-0.788	-1.186	0.886	-0.823
19	30.219	0.009	12272.35	104.612	-1.357	1.021	-0.787	-1.119	0.843	-0.839
20	22.423	0.009	8730.46	74.622	-1.310	0.939	-0.799	-1.133	0.808	-0.842
21	27.854	0.009	14354.80	122.400	-1.313	0.947	-0.800	-1.096	0.779	-0.850
22	31.518	0.009	26306.80	224.412	-1.315	0.957	-0.800	-1.066	0.770	-0.854
23	31.411	0.009	31634.30	269.937	-1.329	0.985	-0.795	-1.082	0.799	-0.849
24	27.056	0.009	21309.25	182.244	-1.326	0.983	-0.795	-1.114	0.823	-0.843
26	26.857	0.009	11790.16	100.968	-1.342	1.010	-0.786	-1.129	0.854	-0.837
27	36.418	0.009	28067.45	239.984	-1.309	0.940	-0.794	-1.022	0.727	-0.865
28	24.118	0.009	7154.34	60.988	-1.352	1.034	-0.782	-1.164	0.890	-0.826
29	33.450	0.009	29897.94	254.927	-1.316	0.978	-0.795	-1.054	0.779	-0.855
30	38.407	0.009	30523.60	260.003	-1.320	0.982	-0.795	-1.020	0.753	-0.863
31	33.689	0.009	27584.16	235.559	-1.314	0.973	-0.795	-1.050	0.773	-0.856

Sin2x										
Run #	Max Runout Distance (cm)	Pixel Area (cm^2)	Zonal Stats (SUM) (cm)	Volume (cm^3)	Point of avulsion			Farthest Downslope Point		
					X	Y	Z	X	Y	Z
3	30.914	0.009	12152.07	103.681	-1.555	1.314	-0.757	-1.428	1.034	-0.778
4	85.952	0.009	146314.06	1259.945	-1.587	1.227	-0.725	-0.915	0.715	-0.885
5	60.436	0.009	93911.87	806.944	-1.529	1.171	-0.754	-1.052	0.813	-0.855
10	32.337	0.009	31686.11	271.506	-1.577	1.212	-0.731	-1.323	1.021	-0.789
11	42.871	0.009	62929.87	539.220	-1.564	1.220	-0.732	-1.230	0.963	-0.812
12	47.257	0.009	52188.48	447.120	-1.586	1.218	-0.728	-1.217	0.937	-0.816
13	63.872	0.009	123267.72	1053.739	-1.569	1.199	-0.723	-1.071	0.821	-0.853
14	93.668	0.009	121875.89	1047.455	-1.590	1.241	-0.721	-0.857	0.685	-0.897
15	9.569	0.009	1190.79	10.189	-1.551	1.154	-0.737	-1.480	1.096	-0.764
16	20.704	0.009	9584.97	81.569	-1.560	1.164	-0.721	-1.401	1.048	-0.787
20	42.559	0.009	51128.70	437.730	-1.578	1.175	-0.731	-1.253	0.912	-0.813
22	37.901	0.009	27650.14	236.640	-1.577	1.177	-0.722	-1.283	0.953	-0.804
25	49.033	0.009	74106.99	632.329	-1.581	1.174	-0.742	-1.199	0.878	-0.826
26	34.330	0.009	32950.96	280.957	-1.605	1.221	-0.727	-1.338	1.014	-0.788
27	43.477	0.009	46841.39	400.173	-1.587	1.180	-0.731	-1.250	0.918	-0.815
29	36.114	0.009	35048.56	301.078	-1.597	1.210	-0.730	-1.314	0.995	-0.797
30	52.056	0.009	47823.87	410.052	-1.613	1.242	-0.721	-1.207	0.932	-0.820
31	45.135	0.009	39870.21	342.453	-1.578	1.187	-0.735	-1.225	0.919	-0.820
32	52.408	0.009	77585.21	665.181	-1.558	1.144	-0.743	-1.146	0.836	-0.840
33	35.189	0.009	32736.41	281.452	-1.605	1.237	-0.722	-1.328	1.031	-0.791

Count of successful trials and observed avulsions

Among 31 successful runs with the sin(1.5x) curve, 25 avulsions were observed. Among 21 successful runs with the sin(2x) curve, 20 avulsions were observed. The sin(0.5x) curve did not produce any successful runs, while the sin(1x) curve could produce one avulsion out of 31 successful runs. The low amount of data derived from the sin(0.5x) and sin(1x) curves does not allow for proper statistical analysis except to define the probability of avulsion. Correlations or t-tests could not be run for sin(0.5x) because of the absence of runout data. Because there is only one value in the sin(1x) group, there is no variability to measure and meaningful results cannot be derived from Pearson correlation or t-tests. Therefore, the sin(0.5x) and sin(1x) curves were disregarded from further analysis with Pearson correlation and t-tests.

Debris-flow runout statistics

Avulsions from the sin(1.5x) curve are generally associated with longer maximum runout distances and greater volumes of flow runout than avulsions from the sin(2x) curve (Table 2; Table 3).

Table 3. Descriptive statistics generated in GraphPad Prism 9.5 for maximum runout distance and volume between sin(1.5x) and sin(2x).

	Sin(1.5x) Max Runout Distance (cm)	Sin(2x) Max Runout Distance (cm)	Sin(1.5x) Volume (cm^3)	Sin(2x) Volume (cm^3)
Number of values	25	20	25	20
Minimum	16.54	9.569	17.95	10.19
25% Percentile	23.96	34.54	55.6	273.9
Median	27.06	43.17	150.2	405.1
75% Percentile	32.53	52.32	237.8	657
Maximum	49.27	93.67	428.3	1260

Mean	28.35	45.79	158.5	480.5
Std. Deviation	7.057	19.62	105.5	339.9
Std. Error of Mean	1.411	4.386	21.1	76.01
Lower 95% CI	25.43	36.61	115	321.4
Upper 95% CI	31.26	54.97	202.1	639.6

Sin(1.5x) and sin(2x) are normally distributed (Table 4), enabling the use of parametric tests for assessing difference.

Table 4. Normality and lognormality tests of runout volumes and distances between sin(1.5x) and sin(2x) from GraphPad Prism 9.5. "*" denotes $P \leq 0.05$; "ns" denotes no significance.

	Sin(1.5x) Max Runout Distance (cm)	Sin(1.5x) Volume (cm^3)	Sin(2x) Max Runout Distance (cm)	Sin(2x) Volume (cm^3)
Probability normal (Gaussian)	23.31%	48.09%	67.13%	81.03%
Probability lognormal	76.69%	51.91%	32.87%	18.97%
Likelihood ratio (LR)	0.3039	0.9263	2.042	4.272
1/LR	3.291	1.08	0.4896	0.2341
Which distribution is more likely?	Lognormal	Lognormal	Normal	Normal
D'Agostino & Pearson test				
K2	7.102	1.162	4.873	3.456
P value	0.0287	0.5592	0.0875	0.1777
Passed normality test (alpha=0.05)?	No	Yes	Yes	Yes
P value summary	*	ns	ns	ns
Anderson-Darling test				
A2*	0.3886	0.5472	0.6073	0.6696
P value	0.3592	0.1432	0.0987	0.0682
Passed normality test (alpha=0.05)?	Yes	Yes	Yes	Yes
P value summary	ns	ns	ns	ns

Shapiro-Wilk test				
W	0.9451	0.9303	0.9306	0.9166
P value	0.1944	0.0881	0.1584	0.0853
Passed normality test (alpha=0.05)?	Yes	Yes	Yes	Yes
P value summary	ns	ns	ns	ns
Number of values	25	25	20	20
Number of zeroes	0	0	0	0
Number of negative values	0	0	0	0

Results of the parametric unpaired t-test with Welch's correction (Table 5; Figure 7) suggest there is a significant difference ($P<0.01$) in volumes observed between sin(1.5x) and sin(2x). Volumes in the sin(1.5x) group cluster in the range of 200 – 300 cm^3, but regularly plot in the range of 20 – 200 cm^3. Volumes in the sin(2x) group largely cluster within the range of 250 – 450 cm^3. Volumes below 250 cm^3 in this group are rare. A supplemental F test of compared variances shows that these two groups are statistically different ($P<0.01$).

Table 5. Parametric unpaired t-test with Welch's correction performed on sin(1.5x) volume vs. sin(2x) volume in GraphPad Prism 9.5. "***" denotes $P \leq 0.001$; "****" denotes $P \leq 0.0001$.

Column headers	
Column D	Sin(2x) Volume (cm^3)
Column B	Sin(1.5x) Volume (cm^3)
Unpaired t test with Welch's correction	
P value	0.005
P value summary	***
Significantly different (P < 0.05)?	Yes
One- or two-tailed P value?	Two-tailed
Welch-corrected t, df	t=4.081, df=21.94
How big is the difference?	
Mean of column B	158.5
Mean of column D	480.5
Difference between means (D - B) ± SEM	321.9 ± 78.88

95% confidence interval	158.3 to 485.6
R squared (eta squared)	0.43
F test to compare variances	
F, DFn, Dfd	10.38, 19, 24
P value	<0.0001
P value summary	****
Significantly different (P < 0.05)?	Yes
Data analyzed	
Sample size, column B	25
Sample size, column D	20

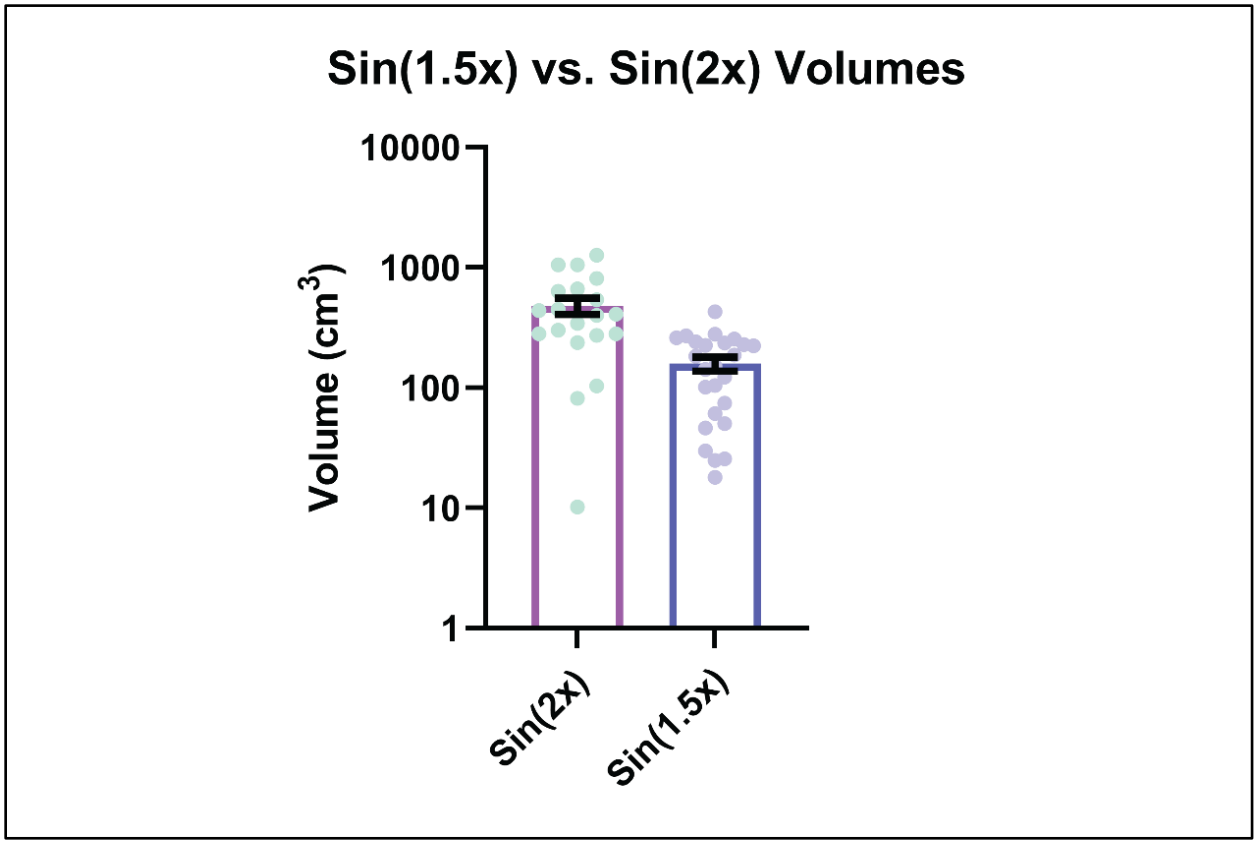

Figure 7. Plot of debris-flow runout volumes observed between the sin(1.5x) and sin(2x) groups. Error bars represent the standard error of the mean (SEM).

Results of the parametric unpaired t-test with Welch's correction (Table 6; Figure 8) suggest there is a significant difference (P < 0.01) in maximum runout distance observed

between sin(1.5x) and sin(2x). Volumes in the sin(1.5x) group clustered from 25 – 30 cm^3, but also were frequently observed to fall within the broader range of 20 – 40 cm^3. Volumes in the sin(2x) group clustered within the 30 – 50 cm^3 range, although they were also frequently observed to fall within the broader range of 30 – 64 cm^3. A supplemental F test of compared variances supports the t-test results showing that these two groups are statistically different (P <0.01).

Table 6. Parametric unpaired t-test with Welch's correction performed on sin(1.5x) maximum runout distance vs. sin(2x) maximum runout distance in GraphPad Prism 9.5. "***" denotes P ≤ 0.001; "****" denotes P ≤ 0.0001.

Column headers	
Column C	Sin(2x) Max Runout Distance (cm)
Column A	Sin(1.5x) Max Runout Distance (cm)
Unpaired t test with Welch's correction	
P value	0.001
P value summary	***
Significantly different (P < 0.05)?	Yes
One- or two-tailed P value?	Two-tailed
Welch-corrected t, df	t=3.785, df=22.94
How big is the difference?	
Mean of column A	28.35
Mean of column C	45.79
Difference between means (C - A) ± SEM	17.44 ± 4.608
95% confidence interval	7.909 to 26.97
R squared (eta squared)	0.3844
F test to compare variances	
F, DFn, Dfd	7.726, 19, 24
P value	<0.0001
P value summary	****
Significantly different (P < 0.05)?	Yes
Data analyzed	
Sample size, column A	25
Sample size, column C	20

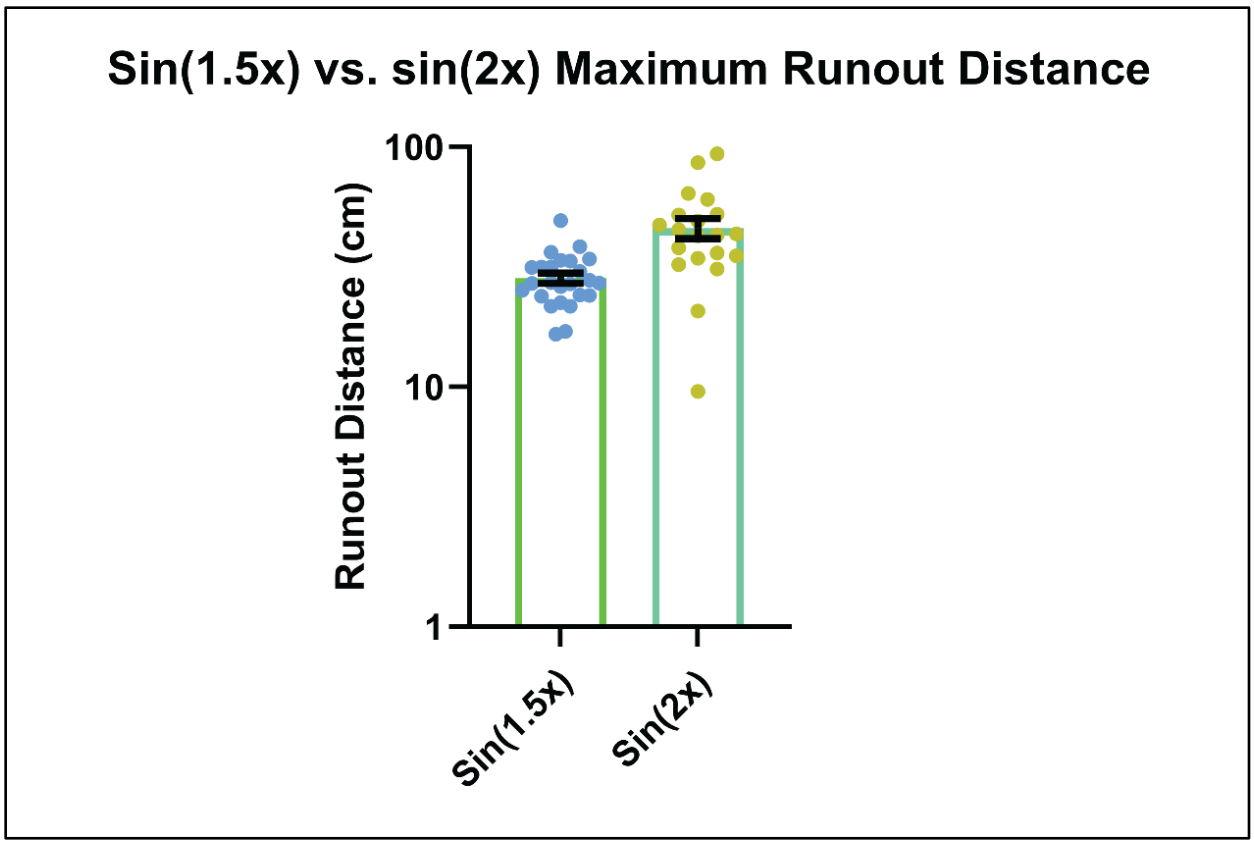

Figure 8. Plot of debris-flow runout maximum distances observed between the sin(1.5x) and sin(2x) groups. Error bars represent the standard error of the mean (SEM).

Results of Pearson correlation suggest there are statistically significant ($P<0.01$) positive relationships between volume and maximum runout distance per study channel. These are elaborated quantitatively with relatively high R^2 values at 0.79 for the sin(1.5x) group and 0.88 for the sin(2x) (Table 7), and qualitatively (Figure 9).

Table 7. Correlation statistics for maximum runout distance vs. volume between sin(1.5x) and sin(2x) from GraphPad Prism 9.5. "****" denotes $P \leq 0.0001$.

	Sin(1.5x) Max Runout Distance (cm) vs. Sin(1.5x) Volume (cm^3)	Sin(2x) Max Runout Distance (cm) vs. Sin(2x) Volume (cm^3)
Pearson r		
r	0.8884	0.936
95% confidence interval	0.7601 to 0.9500	0.8425 to 0.9748
R squared	0.7892	0.8762

P value		
P (two-tailed)	<0.0001	<0.0001
P value summary	****	****
Significant? (alpha = 0.05)	Yes	Yes
Number of XY Pairs	25	20

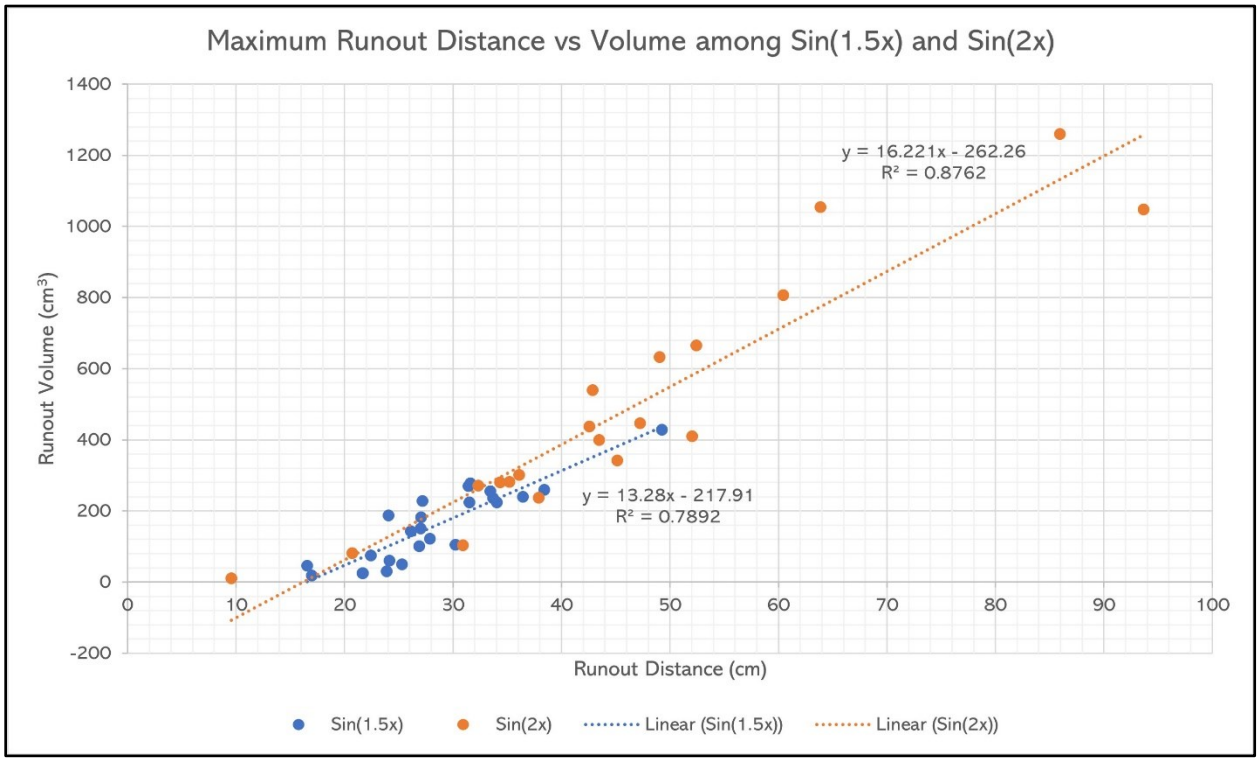

Figure 9. Correlation analysis performed on maximum runout distance and runout volume experienced among the sin(1.5x) and sin(2x) groups.

Debris-flow superelevation

Flow superelevation was observed (though not measured) during the trials and left coatings of muddy debris along the outer bend walls. Video recordings suggest avulsions were the direct result of flow superelevation (Figure 10). Moreover, bank failure because of superelevation was not observed during the experiment.

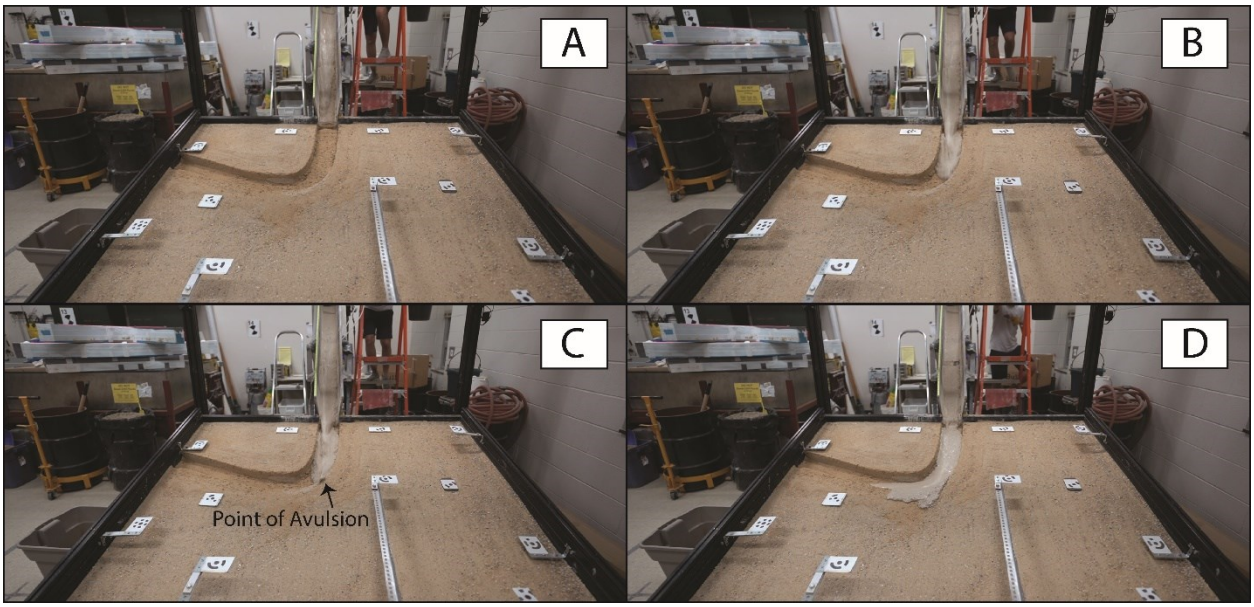

Figure 10. Timeline of debris-flow transport and avulsion in the experimental flume. Frame (A) represents flow during transport in the chut. Frame (B) represents flow during transport in the channel. Frame (C) represents flow avulsion initiation along the channel outer bend. Frame (D) represents the final position of the debris-flow following deposition.

Outer bend profile inundation and points of avulsion

Total inundated area for sin(1.5x) included segments 41 through 65 +/- 2 segments (representing 24% +/- 2% of the curve), and total inundated area for sin(2x) included segments 40 through 75 +/- 2 segments (representing 35% +/- 2% of the curve). See Figure 11 for an illustration of inundation overestimation by as much as one segment on either edge of the inundation range (for a total of two segments).

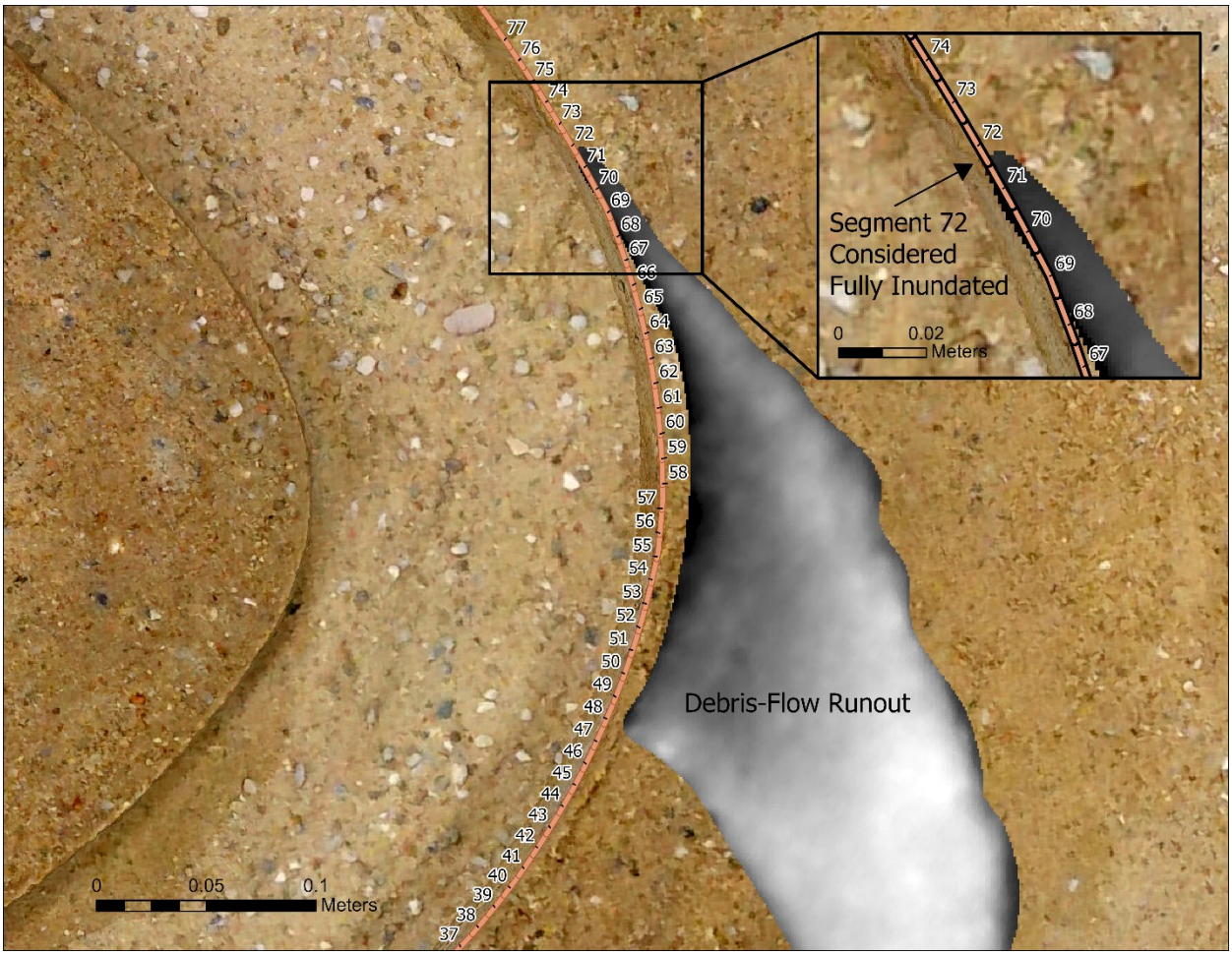

Figure 11. Illustration of outer bend profile inundation overestimation error.

Points of avulsion (uppermost segments of outer bend profile inundation) fell between segments 57 and 65 in the sin(1.5x) group, and segments 60 to 75 in the sin(2x) group (Table 8; Table 9; Figure 12).

Table 8. Outer bend profile inundation ranges. Ranges of inundated segments presented as '**FROM** : **TO (RANGE)**'.

Sin(2x)		Sin(1.5x)	
Run	Inundated segments	Run	Inundated segments
3	47 : 60 (13)	3	47 : 62 (15)
4	43 : 72 (29)	4	42 : 61 (19)
5	42 : 64 (22)	5	45 : 62 (17)
10	49 : 68 (19)	7	42 : 60 (18)
11	44 : 72 (28)	8	42 : 61 (19)

12	40 : 66 (26)	9	42 : 60 (18)
13	41 : 69 (28)	10	41 : 59 (18)
14	42 : 73 (31)	11	43 : 64 (21)
15	55 : 63 (8)	12	42 : 60 (18)
16	50 : 64 (14)	14	42 : 60 (18)
20	41 : 66 (25)	15	42 : 59 (17)
22	44 : 67 (23)	17	49 : 65 (16)
25	44 : 65 (21)	18	51 : 63 (12)
26	43 : 70 (27)	19	45 : 61 (16)
27	42 : 66 (24)	20	45 : 62 (17)
29	48 : 71 (23)	21	44 : 61 (17)
30	44 : 75 (31)	22	44 : 57 (13)
31	45 : 69 (24)	23	44 : 61 (17)
32	42 : 68 (26)	24	42 : 61 (19)
33	41 : 72 (31)	26	46 : 65 (19)
--	--	27	46 : 59 (13)
--	--	28	45 : 65 (20)
--	--	29	44 : 60 (16)
--	--	30	43 : 61 (18)
--	--	31	43 : 58 (15)

Table 9. Descriptive statistics generated in GraphPad Prism 9.5 for sin(1.5x) and sin(2x) points of avulsion.

	Sin(1.5x) Points of Avulsion	Sin(2x) Points of Avulsion
Number of values	25	20
Minimum	57.00	60.00
25% Percentile	60.00	65.25
Median	61.00	68.00
75% Percentile	62.00	71.75
Maximum	65.00	75.00
Mean	61.08	68.00
Std. Deviation	2.100	3.839
Std. Error of Mean	0.4200	0.8584
Lower 95% CI	60.21	66.20
Upper 95% CI	61.95	69.80

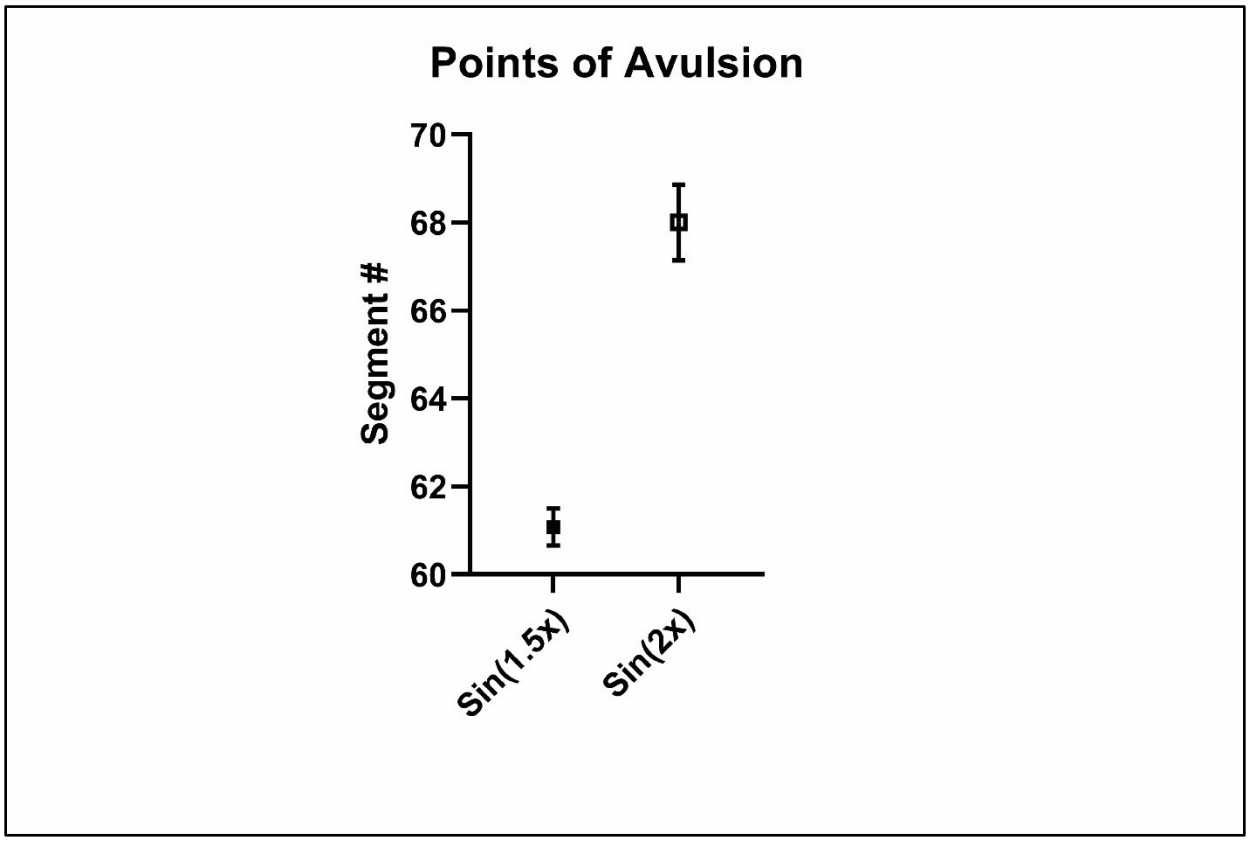

Figure 12. Locations of avulsion initiation between sin(1.5x) and sin(2x) groups, with SEM.

Tests of gaussian distribution for outer bend profile inundation (Table 10) and points of avulsion (Table 11) confirm normality among the datasets, prompting parametric tests for difference.

Table 10. Normality and lognormality tests of outer bend profile inundation ranges between sin(1.5x) and sin(2x) from GraphPad Prism 9.5. "*" denotes $P \leq 0.05$; "ns" denotes no significance.

	Sin(1.5x) Outer Bend Profile Segment Inundation Range	Sin(2x) Outer Bend Profile Segment Inundation Range
Probability normal (Gaussian)	23.31%	98.50%
Probability lognormal	76.69%	1.50%

Likelihood ratio (LR)	0.3039	65.73
1/LR	3.291	0.01521
Which distribution is more likely?	Lognormal	Normal
D'Agostino & Pearson test		
K2	7.102	5.405
P value	0.0287	0.067
Passed normality test (alpha=0.05)?	No	Yes
P value summary	*	ns
Anderson-Darling test		
A2*	0.3886	0.6365
P value	0.3592	0.083
Passed normality test (alpha=0.05)?	Yes	Yes
P value summary	ns	ns
Shapiro-Wilk test		
W	0.9451	0.9043
P value	0.1944	0.0497
Passed normality test (alpha=0.05)?	Yes	No
P value summary	ns	*
Number of values	25	20
Number of zeroes	0	0
Number of negative values	0	0

Table 11. Normality and lognormality tests of points of avulsion between sin(1.5x) and sin(2x) from GraphPad Prism 9.5. "*" denotes $P \leq 0.05$; "ns" denotes no significance.

	Sin(1.5x) Points of Avulsion	Sin(2x) Points of Avulsion
Probability normal (Gaussian)	46.34%	52.29%

Probability lognormal	53.66%	47.71%
Likelihood ratio (LR)	0.8635	1.096
1/LR	1.158	0.9125
Which distribution is more likely?	Lognormal	Normal
D'Agostino & Pearson test		
K2	0.9037	0.1813
P value	0.6364	0.9133
Passed normality test (alpha=0.05)?	Yes	Yes
P value summary	ns	ns
Anderson-Darling test		
A2*	0.6741	0.1865
P value	0.0689	0.8922
Passed normality test (alpha=0.05)?	Yes	Yes
P value summary	ns	ns
Shapiro-Wilk test		
W	0.9375	0.9821
P value	0.1299	0.9579
Passed normality test (alpha=0.05)?	Yes	Yes
P value summary	ns	ns
Number of values	25	20
Number of zeroes	0	0
Number of negative values	0	0

Results of the parametric unpaired t-test with Welch's correction (Table 12) suggest a significant difference ($P<0.01$) in outer bend profile segment inundation ranges observed between sin(1.5x) and sin(2x). A supplemental F test of compared variances supports this conclusion ($P<0.01$).

Table 12. Parametric unpaired t-test with Welch's correction performed on sin(1.5x) outer bend profile segment inundation range vs. sin(2x) outer bend profile segment inundation range in GraphPad Prism 9.5. "***" denotes P ≤ 0.001; "****" denotes P ≤ 0.0001.

Column headers	
Column H	Sin(2x) Segment Inundation Range
Column D	Sin(1.5x) Segment Inundation Range
Unpaired t test with Welch's correction	
P value	0.0002
P value summary	***
Significantly different (P < 0.05)?	Yes
One- or two-tailed P value?	Two-tailed
Welch-corrected t, df	t=4.529, df=22.77
How big is the difference?	
Mean of column D	17.04
Mean of column H	23.65
Difference between means (H - D) ± SEM	6.610 ± 1.459
95% confidence interval	3.589 to 9.631
R squared (eta squared)	0.474
F test to compare variances	
F, DFn, Dfd	8.093, 19, 24
P value	<0.0001
P value summary	****
Significantly different (P < 0.05)?	Yes
Data analyzed	
Sample size, column D	25
Sample size, column H	20

Results of the parametric unpaired t-test with Welch's correction (Table 13) suggests a significant difference (P<0.01) in points of avulsion between sin(1.5x) and sin(2x). A supplemental F test of compared variances supports the t-test results (P<0.01).

Table 13. Parametric unpaired t-test with Welch's correction performed on sin(1.5x) points of avulsion vs. sin(2x) points of avulsion in GraphPad Prism 9.5. "**" denotes P ≤ 0.01; "****" denotes P ≤ 0.0001.

Column headers

Column G	Sin(2x) Points of Avulsion
Column B	Sin(1.5x) Points of Avulsion
Unpaired t test with Welch's correction	
P value	<0.0001
P value summary	****
Significantly different (P < 0.05)?	Yes
One- or two-tailed P value?	Two-tailed
Welch-corrected t, df	t=7.241, df=27.92
How big is the difference?	
Mean of column B	61.08
Mean of column G	68.00
Difference between means (G - B) ± SEM	6.920 ± 0.9556
95% confidence interval	4.962 to 8.878
R squared (eta squared)	0.6525
F test to compare variances	
F, DFn, Dfd	3.342, 19, 24
P value	0.0060
P value summary	**
Significantly different (P < 0.05)?	Yes
Data analyzed	
Sample size, column B	25
Sample size, column G	20

Outer bend profile inundation vs. debris-flow runout

From a visual perspective, the 81 – 100% zone of likelihood of inundation for the outer bend matches closely with the 81 – 100% zone for inundation of the alluvial bed from runout (Figure 13, Figure 14).

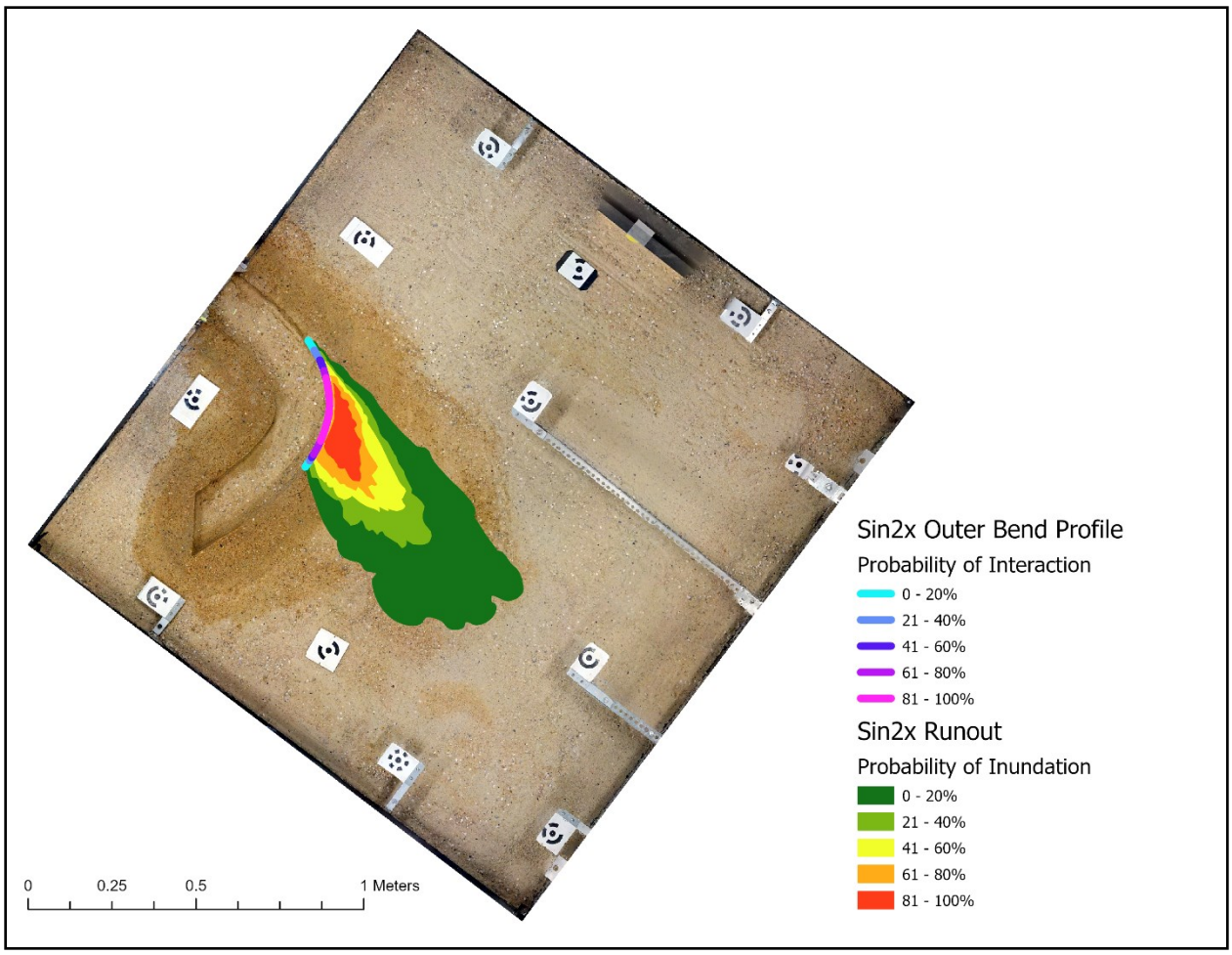

Figure 13. Sin(2x) zones of probability for outer bend profile interaction and outflow plain inundation resulting from debris-flow runout.

Figure 14. Sin(1.5x) zones of probability for outer bend profile interaction and outflow plain inundation resulting from debris-flow runout.

Results of Pearson correlation for the sin(1.5x) group show that outer bend profile segment inundation is not significantly related to debris-flow runout volumes (Table 14) nor debris-flow runout maximum distances (Table 15) (Figure 15). However, Pearson correlations for the sin(2x) group show a weak ($R^2 = 0.36$) but significant ($P<0.01$) relationship between outer bend profile segment inundation range and debris-flow runout volumes (Table 16), and a weak ($R^2 = 0.47$) but significant ($P<0.01$) relationship between outer bend profile segment inundation range and debris-flow runout maximum distances (Table 17) (Figure 15).

Table 14. Pearson correlation performed on sin(1.5x) outer bend profile segment inundation range vs. sin(1.5x) debris-flow runout volume in GraphPad Prism 9.5. “ns” denotes no significance.

Sin(1.5x) Volume (cm^3) vs. Sin(1.5x) Segment Inundation Range	
Pearson r	
r	0.05504
95% confidence interval	-0.3477 to 0.4406
R squared	0.00303
P value	
P (two-tailed)	0.7938
P value summary	ns
Significant? (alpha = 0.05)	No
Number of XY Pairs	25

Table 15. Pearson correlation performed on sin(1.5x) outer bend profile segment inundation range vs. sin(1.5x) maximum debris-flow runout distance in GraphPad Prism 9.5. “ns” denotes no significance.

Sin(1.5x) Maximum Runout Distance (cm) vs. Sin(1.5x) Segment Inundation Range	
Pearson r	
r	0.03677
95% confidence interval	-0.3636 to 0.4257
R squared	0.001352
P value	
P (two-tailed)	0.8615
P value summary	ns
Significant? (alpha = 0.05)	No
Number of XY Pairs	25

Table 16. Pearson correlation performed on sin(2x) outer bend profile segment inundation range vs. sin(2x) debris-flow volume. "**" denotes $P \leq 0.01$.

Sin(2x) Volume (cm^3) vs. Sin(2x) Segment Inundation Range	
Pearson r	
r	0.6015
95% confidence interval	0.2167 to 0.8246
R squared	0.3618
P value	
P (two-tailed)	0.005
P value summary	**
Significant? (alpha = 0.05)	Yes
Number of XY Pairs	20

Table 17. Pearson correlation performed on sin(2x) outer bend profile segment inundation range vs. sin(2x) debris-flow runout maximum distance in GraphPad Prism 9.5. "***" denotes $P \leq 0.001$.

Sin(2x) Segment Inundation Range vs. Sin(2x) Maximum Runout Distance (cm)	
Pearson r	
r	0.6829
95% confidence interval	0.3445 to 0.8643
R squared	0.4664
P value	
P (two-tailed)	0.0009
P value summary	***
Significant? (alpha = 0.05)	Yes
Number of XY Pairs	20

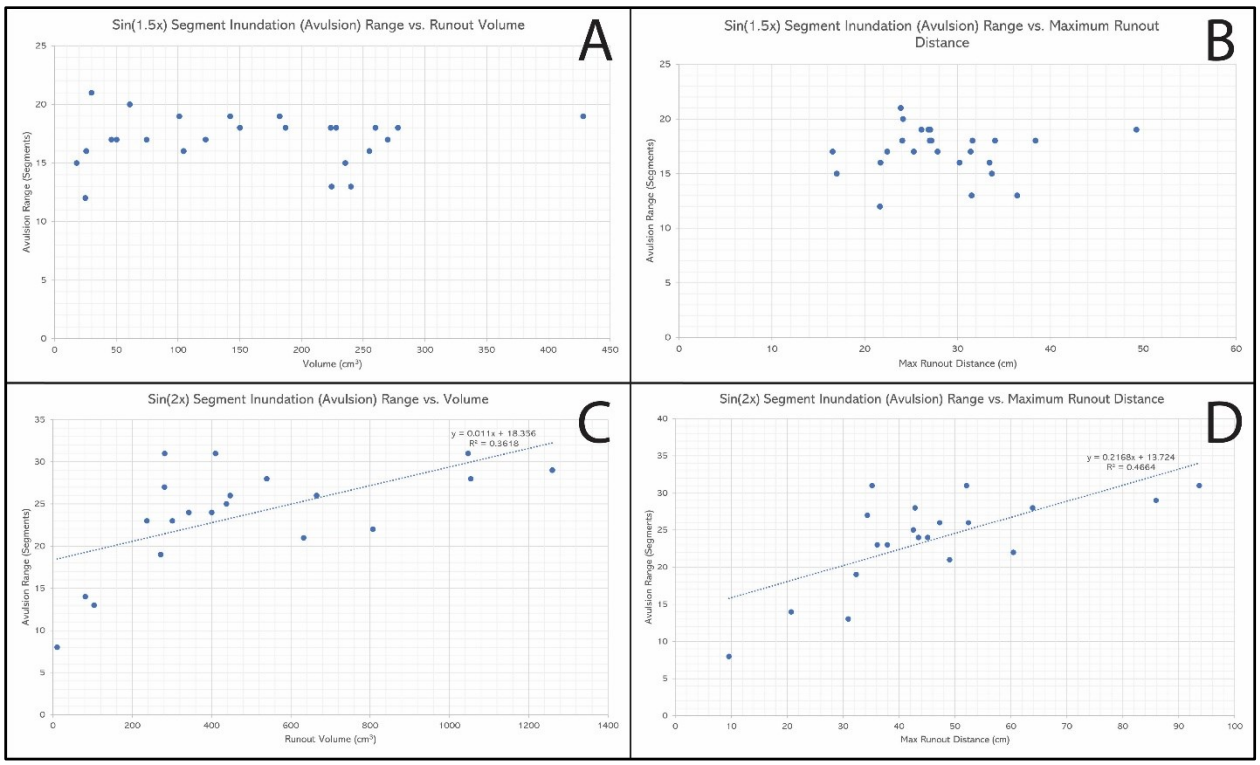

Figure 15. Correlation analysis performed on A) sin(1.5x) avulsion range vs. runout volume; B) sin(1.5x) avulsion range vs. maximum runout distance; C) sin(2x) avulsion range vs. runout volume; and D) sin(2x) avulsion range vs. maximum runout distance.

Points of avulsion vs. debris-flow runout

Results of Pearson correlation for the sin(1.5x) group suggests a weak ($R^2 = 0.31$) but significant ($P<0.01$) relationship between points of avulsion and debris-flow runout volumes (Table 18), but no significant correlation with maximum runout distances (Table 19). The opposite is observed for the sin(2x) group, where points of avulsion are not correlated with debris-flow runout volumes (Table 20) but are potentially weakly correlated ($R^2 =0.24$; $P<0.05$) with maximum runout distances (Table 21). Qualitatively, runout volumes and points of avulsion in the sin(1.5x) group appear to be inversely related, and the opposite observation of correlation existing in runout distances and points of avulsion in the sin(2x) is also observed (Figure 16).

Table 18. Pearson correlation performed on sin(1.5x) points of avulsion vs. sin(1.5x) debris-flow runout volume in GraphPad Prism 9.5. "**" denotes $P \leq 0.01$.

Sin(1.5x) Volume (cm^3) vs. Sin(1.5x) Points of Avulsion	
Pearson r	
r	-0.5587
95% confidence interval	-0.7813 to -0.2099
R squared	0.3121
P value	
P (two-tailed)	0.0037
P value summary	**
Significant? (alpha = 0.05)	Yes
Number of XY Pairs	25

Table 19. Pearson correlation performed on sin(1.5x) points of avulsion vs. sin(1.5x) debris-flow runout maximum distance in GraphPad Prism 9.5. "ns" denotes no significance.

Sin(1.5x) Maximum Runout Distance (cm) vs. Sin(1.5x) Points of Avulsion	
Pearson r	
r	-0.3397
95% confidence interval	-0.6479 to 0.06400
R squared	0.1154
P value	
P (two-tailed)	0.0966
P value summary	ns
Significant? (alpha = 0.05)	No
Number of XY Pairs	25

Table 20. Pearson correlation performed on sin(2x) points of avulsion vs. sin(2x) debris-flow runout volume in GraphPad Prism 9.5. “ns” denotes no significance.

Sin(2x) Volume (cm^3) vs. Sin(2x) Points of Avulsion	
Pearson r	
r	0.4095
95% confidence interval	-0.04029 to 0.7213
R squared	0.1677
P value	
P (two-tailed)	0.0730
P value summary	ns
Significant? (alpha = 0.05)	No
Number of XY Pairs	20

Table 21. Pearson correlation performed on sin(2x) outer bend profile segment inundation range vs. sin(2x) debris-flow runout maximum distance in GraphPad Prism 9.5. “*” denotes $P \leq 0.05$.

Sin(2x) Maximum Runout Distance (cm) vs. Sin(2x) Point of Avulsion	
Pearson r	
r	0.4917
95% confidence interval	0.06287 to 0.7673
R squared	0.2418
P value	
P (two-tailed)	0.0277
P value summary	*
Significant? (alpha = 0.05)	Yes
Number of XY Pairs	20

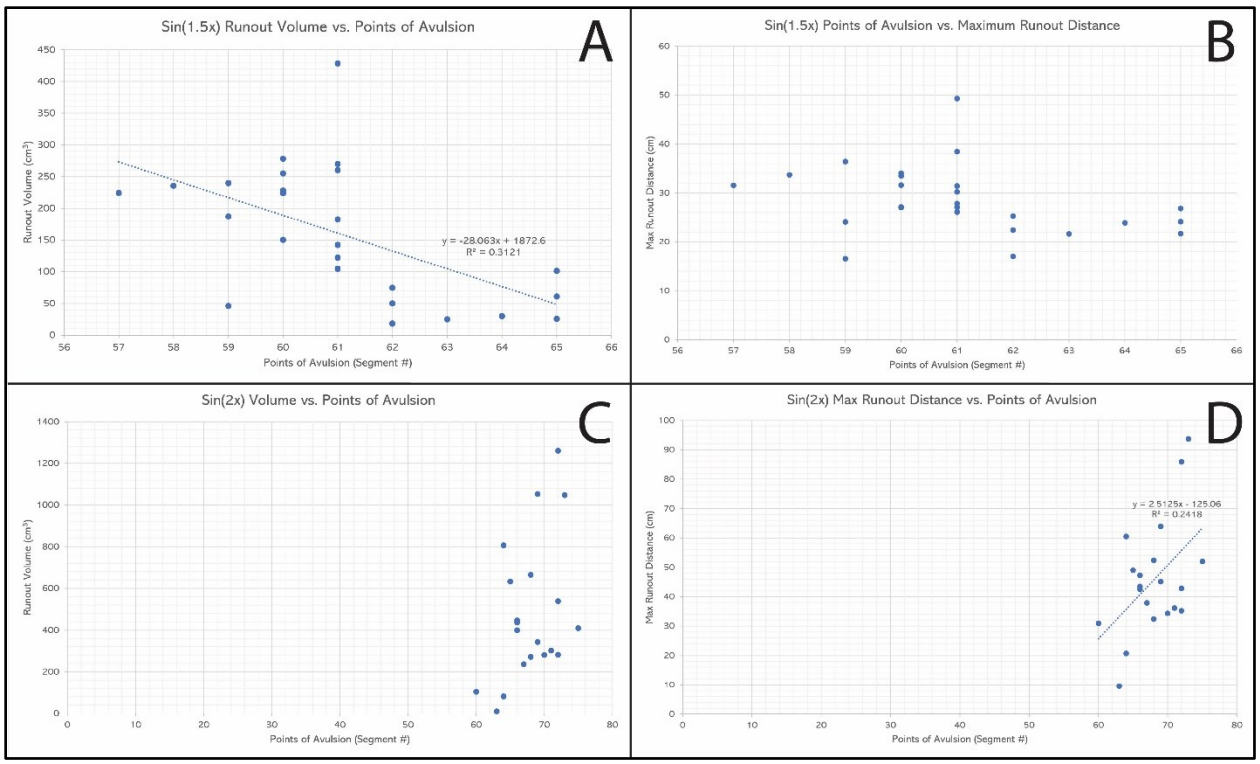

Figure 16. Correlation analysis performed on A) sin(1.5x) points of avulsion vs. runout volume; B) sin(1.5x) points of avulsion vs. maximum runout distance; C) sin(2x) points of avulsion vs. runout volume; and D) sin(2x) points of avulsion vs. maximum runout distance.

Summary

Ranges in avulsion region, and location of avulsion initiation, are statistically different between sin(1.5x) and sin(2x). Avulsion region is statistically unrelated to runout volumes and maximum runout distances in the sin(1.5x) group, though is statistically related to both variables in the sin(2x) group. Locations where avulsions initiate are weakly related to runout volumes, but statistically unrelated to maximum runout distance, in the sin(1.5x) group. The inverse is observed in the sin(2x) group; there, location of avulsion initiation is statistically unrelated to runout volume though weakly related to maximum runout distances.

Measured error

Outflow plain position

Maximum observed error was 0.85 cm, 1.22 cm, and 0.7 cm for X, Y, and Z, respectively (Table 22). As mentioned previously, these coordinates were taken with the explicit purpose of elaborating possible Z offsets between DEMs handled in ArcGIS Pro. While the reported X and Y coordinate values should not be disregarded, small (<2 cm) inconsistencies in placement are of lesser concern.

Table 22. Average corner coordinates and associated error based on a random sample of 'after' scans in Agisoft Metashape.

Run (after)	Metashape Sand Corner Coordinates (m)			
	Upper Left			Upper Right
	X	Y	Z	X
Sin(1.5x)20	-2.448801	0.65457	-0.665	-1.31272
Sin(1.5x)31	-2.445289	0.65491	-0.665	-1.314825
Sin(1.5x)5	-2.445298	0.657629	-0.667	-1.309987
Sin(1.5x)24	-2.447979	0.653025	-0.665	-1.312569
RANGE	**0.003512**	**0.004604**	**0.002**	**0.004838**
AVERAGE	**-2.4468175**	**0.650335**	**-0.6655**	**-1.31252525**
Sin(1x)13	-2.472292	0.643711	-0.674	-1.328854
Sin(1x)4	-2.473513	0.644843	-0.667	-1.326707
Sin(1x)19	-2.472575	0.644359	-0.667	-1.326918
Sin(1x)24	-2.47165	0.642602	-0.669	-1.326143
RANGE	**0.001863**	**0.002241**	**0.007**	**0.002711**
AVERAGE	**-2.4725075**	**0.6438875**	**-0.66925**	**-1.3271555**
Sin(2x)5	-2.433947	0.65359	-0.678	-1.309368
Sin(2x)10	-2.43142	0.6614	-0.677	-1.309906
Sin(2x)26	-2.43993	0.664431	-0.672	-1.31237
Sin(2x)22	-2.432135	0.658922	-0.678	-1.313767
RANGE	**0.00851**	**0.010841**	**0.006**	**0.004399**
AVERAGE	**-2.434358**	**0.6595875**	**-0.67625**	**-1.31135275**

		Lower Left			Lower Right		
Y	Z	X	Y	Z	X	Y	Z
2.178867	-0.642	-1.00523	-0.42564	-1.01	0.129196	1.089171	-0.975
2.176147	-0.643	-1.00503	-0.42787	-1.008	0.129917	1.083725	-0.974
2.181636	-0.64	-0.99889	-0.42738	-1.007	0.12796	1.084192	-0.976
2.185981	-0.641	-1.00412	-0.43765	-1.012	0.131534	1.087262	-0.976
0.009834	**0.003**	**0.006342**	**0.012011**	**0.005**	**0.003574**	**0.005446**	**0.002**
2.1806578	**-0.6415**	**-1.00331**	**-0.42963**	**-1.00925**	**0.129652**	**1.086088**	**-0.97525**
2.188279	-0.645	-1.00288	-0.44045	-1.016	0.133581	1.088556	-0.983
2.192638	-0.644	-1.00254	-0.45261	-1.012	0.132734	1.077983	-0.988
2.192802	-0.642	-1.00192	-0.44989	-1.011	0.134276	1.080762	-0.984
2.189186	-0.641	-1.006	-0.44433	-1.012	0.134887	1.085579	-0.984
0.004523	**0.004**	**0.004078**	**0.01216**	**0.005**	**0.002153**	**0.010573**	**0.005**
2.1907263	**-0.643**	**-1.00333**	**-0.44682**	**-1.01275**	**0.13387**	**1.08322**	**-0.98475**
2.185283	-0.656	-1.0033	-0.42922	-1.003	0.135992	1.078666	-0.988
2.185253	-0.655	-1.00191	-0.4293	-1.007	0.132025	1.084643	-0.988
2.18064	-0.658	-1.00136	-0.42212	-1.006	0.127493	1.085131	-0.988
2.186425	-0.657	-0.99814	-0.42109	-1.01	0.130905	1.081327	-0.99
0.005785	**0.003**	**0.005161**	**0.008215**	**0.007**	**0.008499**	**0.006465**	**0.002**
2.1844003	**-0.6565**	**-1.00118**	**-0.42543**	**-1.0065**	**0.131604**	**1.082442**	**-0.9885**

Alignment error

Maximum and minimum error observed in the sin(1.5x) group were about 0.28 cm and 0.12 cm, respectively (Table 23). Maximum and minimum error observed in the sin(2x) group were about 0.75 cm and 0.6 cm, respectively (Figure 17).

Table 23. Max control point error identified between the "baseline" and ‘after’ scans of each run, determined in Agisoft Metashape.

Sin(1.5x)			
Run #	Error (baseline) (cm)	Error (after) (cm)	Error (max) (cm)
3	0.1457	0.1421	0.1457
4	0.1477	0.1438	0.1477
5	0.1518	0.1437	0.1518
7	0.138	0.1403	0.1403
8	0.2803	0.2806	0.2806
9	0.2699	0.2726	0.2726
10	0.2492	0.2431	0.2492
11	0.2464	0.247	0.247
12	0.2438	0.2417	0.2438
14	0.2446	0.2449	0.2449
15	0.247	0.2434	0.247
17	0.2463	0.2497	0.2497
18	0.2483	0.2447	0.2483
19	0.2484	0.2486	0.2486
20	0.2481	0.2488	0.2488
21	0.2453	0.2449	0.2453
22	0.2462	0.2465	0.2465
23	0.2434	0.2403	0.2434
24	0.2396	0.2393	0.2396
26	0.1239	0.1032	0.1239
27	0.1236	0.0932	0.1236
28	0.1456	0.1519	0.1519
29	0.1471	0.1508	0.1508
30	0.1493	0.1476	0.1493
31	0.1482	0.1546	0.1546
MAXIMUM	**0.2803**	**0.2806**	**0.2806**
MINIMUM	**0.1236**	**0.0932**	**0.1236**
Sin(2x)			
Run #	Error (baseline) (cm)	Error (after) (cm)	Error (max) (cm)

3	0.6138	0.6096	0.6138
4	0.6031	0.5872	0.6031
5	0.6359	0.6481	0.6481
10	0.6251	0.6415	0.6415
11	0.6239	0.6426	0.6426
12	0.6277	0.6403	0.6403
13	0.6451	0.6613	0.6613
14	0.7292	0.7494	0.7494
15	0.632	0.6362	0.6362
16	0.6293	0.6282	0.6293
20	0.6519	0.6544	0.6544
22	0.6481	0.6496	0.6496
25	0.6463	0.648	0.648
26	0.6479	0.6454	0.6479
27	0.6474	0.6502	0.6502
29	0.6502	0.6505	0.6505
30	0.6501	0.6689	0.6689
31	0.6683	0.6681	0.6683
32	0.6683	0.6699	0.6699
33	0.667	0.6681	0.6681
MAXIMUM	**0.7292**	**0.7494**	**0.7494**
MINIMUM	**0.6031**	**0.5872**	**0.6031**

Figure 17. Visualization of GCP displacement from experiment start to finish. Check points and control points mark GCP positions during the final trial; shape of error trail shows distance traveled since first trial.

Outer bend profile inundation error

Maximum error in outer bend profile inundation is estimated to be 7.04 cm along the sin(2x) profile, and 10.09 cm along the sin(1.5x) profile, if dealing with either entire profile (Table 24). However, working with smaller subsets of these profiles yields smaller error. For instance, the maximum error associated with sin(2x) Trial 12 is 5.67 cm as it only deals with 27

segments (27%) out of the total of 100 (100% of the curve). These estimations were produced assuming the extra two segments maintain the greatest observed lengths from their respective profiles (roughly 1.14 cm for sin(2x) and 1.77 cm for sin(1.5x)). Ultimately, increases in associated error could hypothetically be associated with increases in number of inundated segments. However, further determinations of error for each trial among the sin(1.5x) and sin(2x) datasets were not conducted here.

Table 24. Outer bend profile segment size distribution.

Sin(2x)		Sin(1.5x)	
Segment	Length (cm)	Segment	Length (cm)
1	1.1360	1	1.7621
2	1.1321	2	1.7641
3	1.1374	3	1.7587
4	1.1268	4	1.7617
5	1.1388	5	1.7649
6	1.1353	6	1.7649
7	1.1321	7	1.7545
8	1.1374	8	1.7630
9	1.1290	9	1.7665
10	1.1344	10	1.7665
11	1.1316	11	1.7564
12	1.1372	12	1.7650
13	1.1289	13	1.7551
14	1.1346	14	1.7639
15	1.1323	15	1.7590
16	1.1300	16	1.7678
17	1.1360	17	1.7582
18	1.1360	18	1.7671
19	1.1341	19	1.7630
20	1.1323	20	1.7551
21	1.1323	21	1.7650
22	1.1307	22	1.7614
23	1.1370	23	1.7682
24	1.1357	24	1.7564
25	1.1281	25	1.7671
26	1.1345	26	1.7557
27	1.1336	27	1.7667

28	1.1336	28	1.7614
29	1.1395	29	1.7589
30	1.1254	30	1.7682
31	1.1390	31	1.7521
32	1.1317	32	1.7700
33	1.1315	33	1.7603
34	1.1385	34	1.7586
35	1.1314	35	1.7695
36	1.1316	36	1.7541
37	1.1322	37	1.7658
38	1.1357	38	1.7648
39	1.1307	39	1.7555
40	1.1360	40	1.7680
41	1.1372	41	1.7564
42	1.1290	42	1.7618
43	1.1353	43	1.7700
44	1.1287	44	1.7532
45	1.1406	45	1.7671
46	1.1226	46	1.7614
47	1.1413	47	1.7624
48	1.1292	48	1.7666
49	1.1365	49	1.7556
50	1.1322	50	1.7626
51	1.1323	51	1.7611
52	1.1332	52	1.7657
53	1.1327	53	1.7564
54	1.1378	54	1.7601
55	1.1298	55	1.7582
56	1.1344	56	1.7631
57	1.1317	57	1.7596
58	1.1404	58	1.7627
59	1.1328	59	1.7665
60	1.1353	60	1.7617
61	1.1300	61	1.7641
62	1.1344	62	1.7640
63	1.1316	63	1.7612
64	1.1281	64	1.7614
65	1.1402	65	1.7623
66	1.1360	66	1.7586
67	1.1289	67	1.7618
68	1.1330	68	1.7648

69	1.1382	69	1.7622
70	1.1229	70	1.7607
71	1.1374	71	1.7611
72	1.1337	72	1.7608
73	1.1353	73	1.7678
74	1.1321	74	1.7607
75	1.1344	75	1.7607
76	1.1316	76	1.7608
77	1.1346	77	1.7680
78	1.1323	78	1.7541
79	1.1360	79	1.7557
80	1.1345	80	1.7683
81	1.1328	81	1.7545
82	1.1322	82	1.7618
83	1.1324	83	1.7692
84	1.1370	84	1.7648
85	1.1390	85	1.7582
86	1.1328	86	1.7698
87	1.1345	87	1.7564
88	1.1315	88	1.7639
89	1.1315	89	1.7669
90	1.1280	90	1.7541
91	1.1360	91	1.7682
92	1.1280	92	1.7582
93	1.1360	93	1.7669
94	1.1293	94	1.7648
95	1.1385	95	1.7586
96	1.1360	96	1.7664
97	1.1300	97	1.7555
98	1.1280	98	1.7632
99	1.1360	99	1.7621
100	1.1360	100	1.7603
COUNT	**100**	**COUNT**	**100**
MAX	**1.1413**	**MAX**	**1.7700**
MIN	**1.1226**	**MIN**	**1.7521**
RANGE	**0.0187**	**RANGE**	**0.0180**

Order effect

Results of Pearson correlation for the sin(1.5x) group show no significant correlations between run # and maximum debris-flow runout distance (Table 25), run # and debris-flow runout volume (Table 26), run # and outer bend profile segment inundation range (Table 27), or run # and points of avulsion (Table 28) (Figure 18). Likewise, Pearson correlations for the sin(2x) group show no significant correlations between run # and maximum debris-flow runout distance (Table 29), run # and debris-flow runout volume (Table 30), run # and outer bend profile segment inundation range (Table 31), or run # and points of avulsion (Table 32) (Figure 19). These data suggest minimal to no presence of order effects throughout the experiment.

Table 25. Pearson correlation performed on sin(1.5x) run # vs. sin(1.5x) maximum runout distance in GraphPad Prism 9.5. "ns" denotes no significance.

Sin(1.5x) Run # vs. Sin(1.5x) Maximum Runout Distance (cm)	
Pearson r	
r	0.1668
95% confidence interval	-0.2444 to 0.5272
R squared	0.02783
P value	
P (two-tailed)	0.4254
P value summary	ns
Significant? (alpha = 0.05)	No
Number of XY Pairs	25

Table 26. Pearson correlation performed on sin(1.5x) run # vs. sin(1.5x) debris-flow runout volume in GraphPad Prism 9.5. "ns" denotes no significance.

Sin(1.5x) Run # vs. Sin(1.5x) Volume (cm^3)
Pearson r

r	0.08904
95% confidence interval	-0.3173 to 0.4677
R squared	0.007928
P value	
P (two-tailed)	0.6721
P value summary	ns
Significant? (alpha = 0.05)	No
Number of XY Pairs	25

Table 27. Pearson correlation performed on sin(1.5x) run # vs. sin(1.5x) outer bend profile segment inundation range in GraphPad Prism 9.5. “ns” denotes no significance.

Sin(1.5x) Run # vs. Sin(1.5x) Segment Inundation Range	
Pearson r	
r	-0.2234
95% confidence interval	-0.5683 to 0.1884
R squared	0.04989
P value	
P (two-tailed)	0.2832
P value summary	ns
Significant? (alpha = 0.05)	No
Number of XY Pairs	25

Table 28. Pearson correlation performed on sin(1.5x) run # vs. sin(1.5x) points of avulsion in GraphPad Prism 9.5. “ns” denotes no significance.

Sin(1.5x) Run # vs. Sin(1.5x) Points of Avulsion	
Pearson r	
r	-0.02193
95% confidence interval	-0.4135 to 0.3765
R squared	0.0004810
P value	

P (two-tailed)	0.9171
P value summary	ns
Significant? (alpha = 0.05)	No
Number of XY Pairs	25

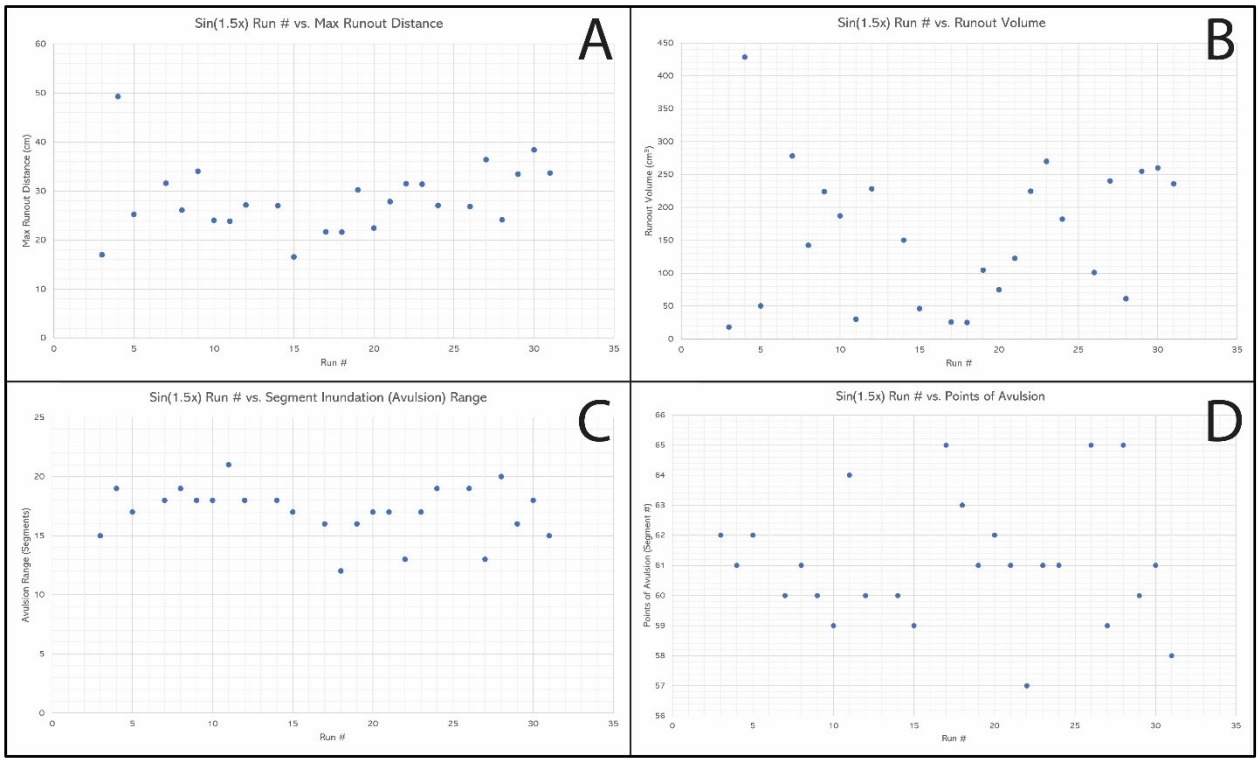

Figure 18. Correlation analysis performed on A) sin(1.5x) run # vs. maximum runout distance; B) sin(1.5x) run # vs. runout volume; C) sin(1.5x) run # vs. avulsion range; and D) sin(1.5x) run # vs. points of avulsion.

Table 29. Pearson correlation performed on sin(2x) run # vs. sin(2x) maximum runout distance in GraphPad Prism 9.5. "ns" denotes no significance.

Sin(2x) Run # vs. Sin(2x) Maximum Runout Distance (cm)	
Pearson r	
r	-0.2089
95% confidence interval	-0.5963 to 0.2574
R squared	0.04363

P value	
P (two-tailed)	0.3768
P value summary	ns
Significant? (alpha = 0.05)	No
Number of XY Pairs	20

Table 30. Pearson correlation performed on sin(2x) run # vs. sin(2x) debris-flow runout volume in GraphPad Prism 9.5. “ns” denotes no significance.

Sin(2x) Run # vs. Sin(2x) Volume (cm^3)	
Pearson r	
r	-0.2875
95% confidence interval	-0.6476 to 0.1777
R squared	0.08263
P value	
P (two-tailed)	0.2191
P value summary	ns
Significant? (alpha = 0.05)	No
Number of XY Pairs	20

Table 31. Pearson correlation performed on sin(2x) run # vs. sin(2x) outer bend profile segment inundation range in GraphPad Prism 9.5. “ns” denotes no significance.

Sin(2x) Run # vs. Sin(2x) Segment Inundation Range	
Pearson r	
r	0.3039
95% confidence interval	-0.1602 to 0.6579
R squared	0.09233
P value	
P (two-tailed)	0.1928
P value summary	ns
Significant? (alpha = 0.05)	No

Number of XY Pairs	20

Table 32. Pearson correlation performed on sin(2x) run # vs. sin(2x) points of avulsion in GraphPad Prism 9.5. “ns” denotes no significance.

Sin(2x) Run # vs. Sin(2x) Points of Avulsion	
Pearson r	
r	0.3575
95% confidence interval	-0.1010 to 0.6907
R squared	0.1278
P value	
P (two-tailed)	0.1218
P value summary	ns
Significant? (alpha = 0.05)	No
Number of XY Pairs	20

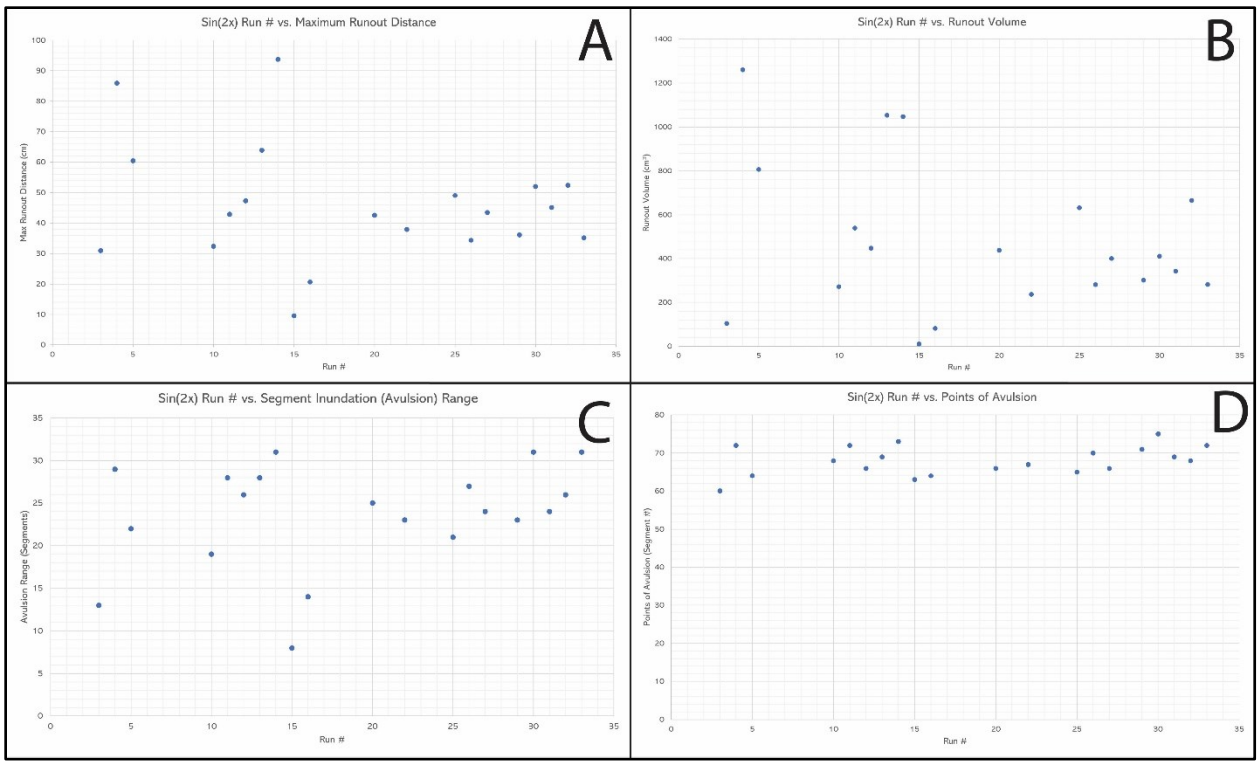

Figure 19. Correlation analysis performed on A) sin(2x) run # vs. maximum runout distance; B) sin(2x) run # vs. runout volume; C) sin(2x) run # vs. avulsion range; and D) sin(2x) run # vs. points of avulsion.

DISCUSSION

Avulsion probability

In the experiments conducted in this study, chances of avulsion were estimated to be 80.7% along the sin(1.5x) channel, 95.2% along the sin(2x) channel, and 3.2% along the sin(1x) channel. These probabilities highlight threats of inundation as a function of curvature and offer meaningful insights from the perspectives of preparedness and mitigation. Regulation of development procedures can be further upgraded to consider threat of debris-flow inundation based on proximity to either channel bend presented in this study. Education of these hazards would be especially useful considering previous opposition to listing debris flows as immediate threats in official building code (McSaveney, 2005).

Debris-flow runout

Given the observations of relationships likely existing between the sin(1.5x) and sin(2x) datasets, it can be inferred that debris-flow runout behavior in the simulated environment is related to channel curvature. To expand on this notion, it appears narrower channel curvatures induce larger areas of debris-flow runout as opposed to wider channel curvatures. This observation is supported by Figure 13 and Figure 14, which depict zones of probability of inundation for the sin(2x) and sin(1.5x) curves, respectively. The implications of these findings include enhanced knowledge for debris-flow runout preparedness if runout behaviors in the natural world mirror those in the lab flume. If so, if the sinuosity of the fan mainstem or other dominant channels on a natural alluvial fan of similar morphology are defined, strategies for evacuation or cordoning-off of hazard regions can be better implemented. These strategies would

hypothetically include the categorization of spatially broader areas as hazard regions where channel curves are narrower (represented by larger values of sinuosity).

Debris-flow superelevation

Video recordings suggest avulsions directly resulted from flow superelevation. Flows were at times capable of climbing the outer wall of either channel to heights exceeding channel depth, and spillover events immediately followed. However, channel bank failure as an immediate result of flow superelevation was not observed in the experiment, contrary to expectations established by Nieto et al. (2022). It is possible that the debris-flow mix worked like concrete and may have cemented the sidewalls against future failures. In support of this hypothesis, after being left to sit for roughly one day or more, the settled and lithified debris-flow runout often withstood light taps with a hammer without deformation. Given the lack of data measured for flow superelevation in this study, no further insights are presented.

Debris-flow avulsions in channels clear of plugs

Video recordings taken with the DSLR camera appeared to show avulsions being initiated by debris-flow fronts. Natural flow fronts tend to consist of the heaviest materials within the debris-flow mass (Iverson, 1997; Davies, 2008), and it is conceivable that the flow fronts in this study may have held the greatest kinetic energies and capacities for evacuation from the channel. These observations add support for the idea that debris-flow avulsions can be initiated in channels free of debris pileup, since pileup could not have occurred ahead of the flow front prior to its transit through the channel. These observations contradict the established literature

(e.g., Davies and McSaveney, 2008; Santi et al., 2017; Leenman and Eaton, 2021) that suggests debris flows may require channel plugs to initiate avulsions. The results of this study suggest that debris flows can avulse from channels free of debris pileup where channel bends are sharp enough to induce steep gradients in flow superelevation and eventual bank overspill.

Outer bend profile inundation and points of avulsion

The range of inundated segments is generally greater among the sin(2x) group than the sin(1.5x) group (Figure 20; Figure 21; Figure 22; Table 33). The reported magnitudes in ranges of inundated segments between the sin(1.5x) and sin(2x) trials, however, may be influenced by segment size. Because the sin(1.5x) outer bend profile curve maintained a longer curve length, its divided segments represented larger areas than the sin(2x) curve after dividing both lengths by 100. Thus, a debris-flow runout event would hypothetically inundate more segments along the sin(2x) bend than the sin(1.5x) bend if replicated and placed atop both profiles. One approach to equate the significance in segment sizes among both profiles would be to derive the averages of both segment size distributions (1.13 cm for the sin(2x) group and 1.76 cm for the sin(1.5x) group), then multiply all values in the sin(2x) group by 1.55. This would horizontally exaggerate the sin(2x) group segment lengths and brings its values closer in significance to the sin(1.5x) group, thus reducing the influence of segment size on avulsion range in the sin(2x) group. However, there is still value to the current configuration. For instance, these two outer bend profile curves are roughly approximated by 180° from start to finish since the curves were cut at their respective sine wave inflection points (effectively creating sine wave half-cycles). Multiplying every segment number among both profiles by 1.8 would derive values consistent with their corresponding degrees out of 180°.

Table 33. Descriptive statistics generated in GraphPad Prism 9.5 for sin(1.5x) and sin(2x) outer bend profile segment inundation ranges.

	Sin(1.5x) Outer Bend Profile Segment Inundation Range	Sin(2x) Outer Bend Profile Segment Inundation Range
Number of values	25	20
Minimum	12.00	8.000
25% Percentile	16.00	21.25
Median	17.00	24.50
75% Percentile	18.50	28.00
Maximum	21.00	31.00
Mean	17.04	23.65
Std. Deviation	2.189	6.226
Std. Error of Mean	0.4377	1.392
Lower 95% CI	16.14	20.74
Upper 95% CI	17.94	26.56

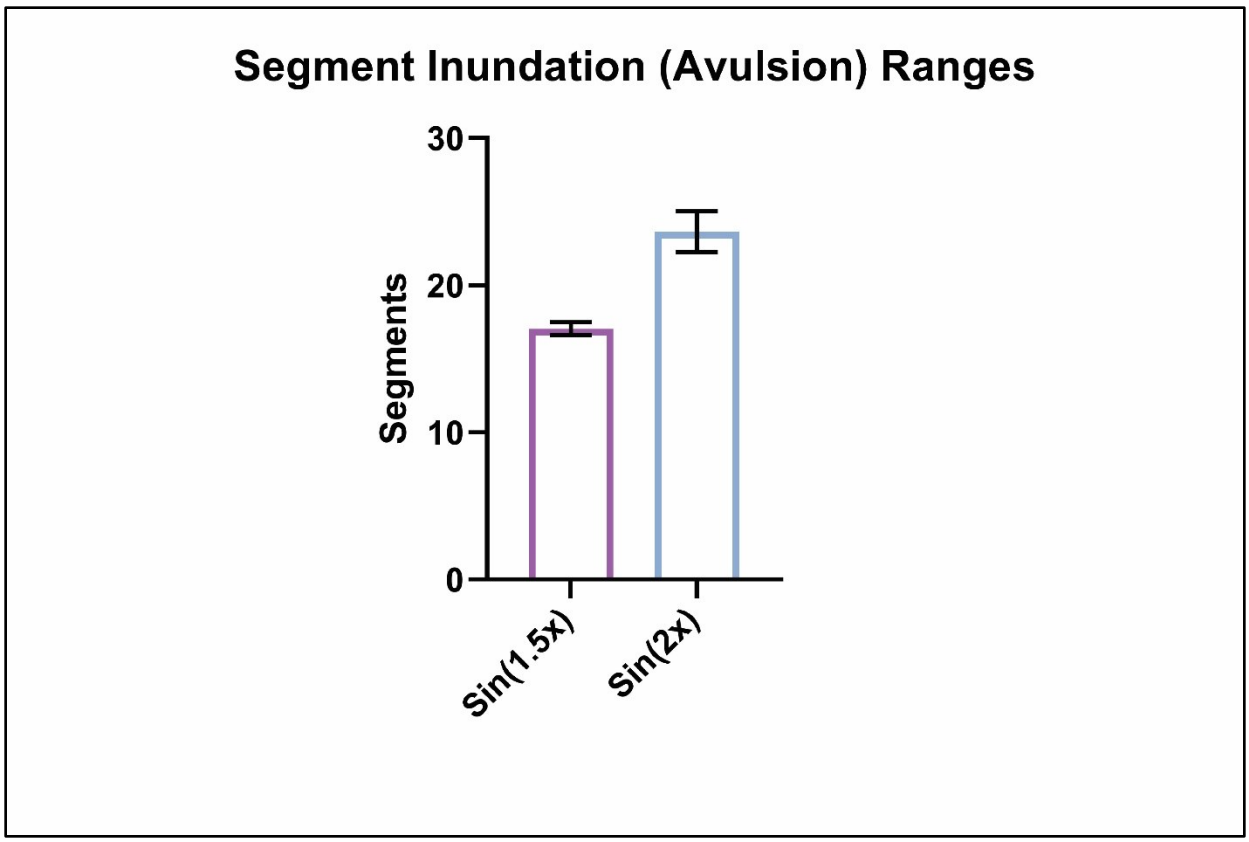

Figure 20. Avulsion ranges between the sin(1.5x) and sin(2x) groups, with SEM.

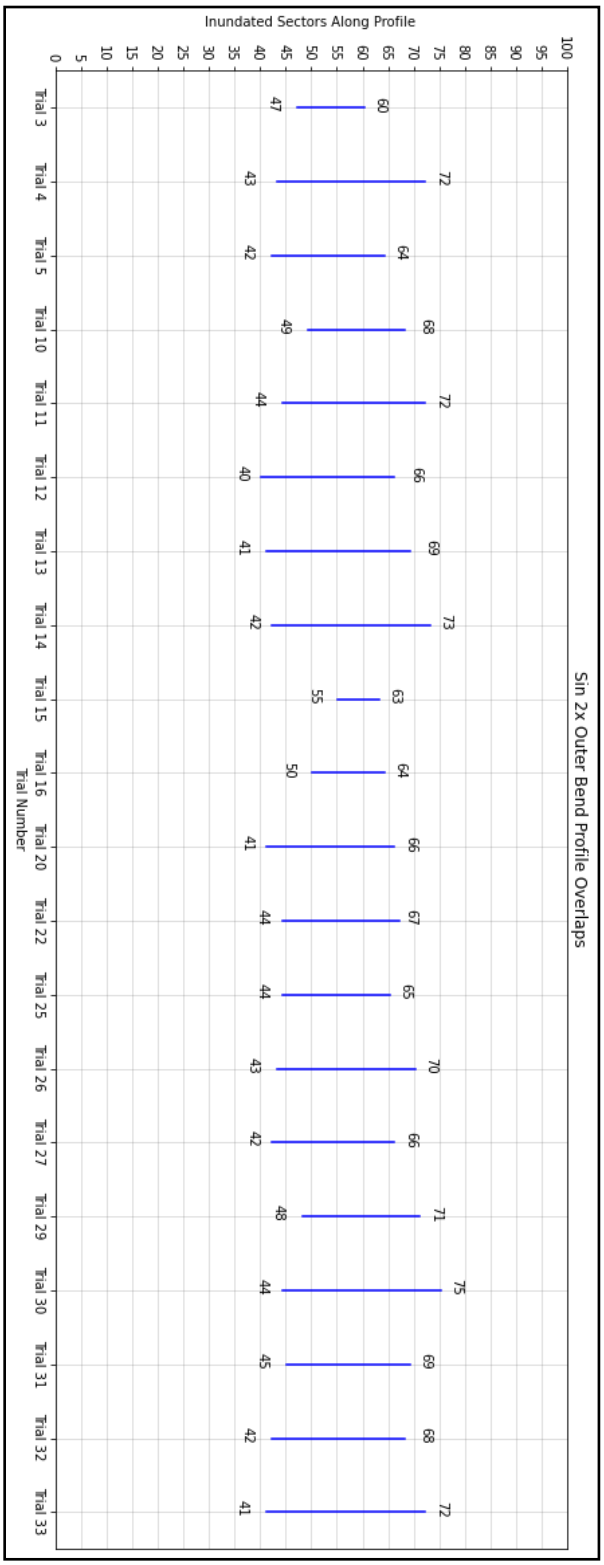

Figure 21. Sin(2x) outer bend profile inundation measured as inundated segments per trial.

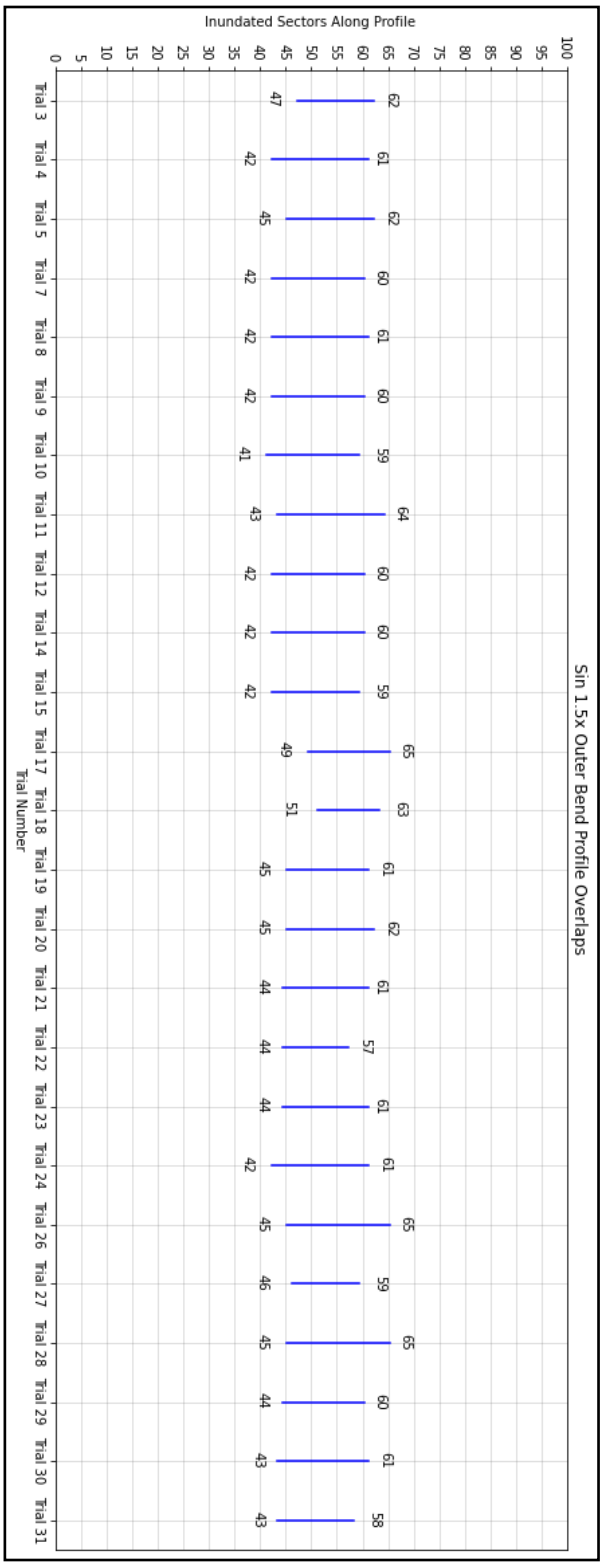

Figure 22. Sin(1.5x) outer bend profile inundation measured as inundated segments per trial.

The observed variations in outer bend profile inundation ranges and avulsion points between sin(1.5x) and sin(2x) suggest variability in outcome with variability in sinuosity. This distinction further supports the idea that debris-flow inundation and runout behaviors in channelized alluvial fan settings are directly influenced by sine curvature.

Outer bend profile inundation vs. debris-flow runout

Results of Pearson correlation suggest that outer bend profile inundation is driven by a mechanism unique from those that influence debris-flow volumes and maximum runout distances between sin(1.5x) and sin(2x). However, the observation of overlap among the zones of likelihood of avulsion between outer bend profiles and their corresponding runout zones may still hold credibility. The Pearson correlation had defined similarity in terms of magnitudes and not spatial overlaps. Therefore, it is still conceivable that zones of likely outer bend profile inundation and alluvial plain inundation are spatially related.

Points of avulsion vs. debris-flow runout

It is uncertain whether location of avulsion initiation points is influenced by a mechanism unique from those that affect debris-flow volumes and maximum runout distances between sin(1.5x) and sin(2x). If these variables were related, it would suggest that the extent of superelevation is related to runout volume and distance, if even just tangentially. This statement follows the logic that superelevation influences whether a flow will avulse, and thus is assumed to be naturally related to where the flow will begin to avulse.

Applications of the study

Results derived from this study are applicable to channel bends of similar angles of curvature on alluvial fans of equal slope. If probable areas of failure within a watershed are detected and the expected volume of flow produced matches that utilized in this research, estimates of debris-flow runout distance and runout volumes can be made if the flows are projected to come across fans and channels with comparable sinuosity to those studied here. Moreover, where natural environments resemble those modeled in this study, control measures to be designed for watershed flood and damage mitigation may benefit from the maps of zones of probable inundation, as well as determinations of likelihoods of avulsion by curvature, presented in this paper. This study demonstrated sharp-angled meander bends on simulated alluvial fans are more prone to excessive superelevation and eventual avulsion. Therefore, the necessary deployment of flood control measures such as debris barrier walls could be done more strategically and cost-effectively by targeting those regions most prone to spillover events, either keeping the debris-flow confined to the channel or protecting downfan regions from runout.

Further testing with a wider assortment of channels of differing sinuosity could have possibly provided the opportunity to produce rating curves between sinuosity and debris-flow runout and inundation behaviors; these rating curves would then expand the applicability of the model to beyond scenarios where parameters must match those studied or accounted for in this experiment.

Error

Alignment error

Estimated error (mostly XY translation errors) resulting from improper GCP placement appear to be related to the time elapsed between the trial run and the moment of image capture with the TLS. For instance, the GCP reference coordinates were obtained for the final arrangement of GCPs following the sin(1.5x) trials of the experiment, and the timescale of trial completion during the experiment followed the sequence, from first to last, of sin(2x), sin(1x), and sin(1.5x). When assessing error across the three curves, the least observed error lies with the sin(1.5x) series of Agisoft Metashape projects, and the most observed error lies with the sin(2x) series of projects. Nonetheless, XY translation errors are of small concern when assessing volumes and runout distances. It was observed that 'before' and 'after' pairs for each trial were positioned optimally above each other regardless of alignment error, and it is assumed that the errors were attributed to both in the same fashion, thus negating the effect. This was relevant when preparing DoDs for volumetric analysis. Otherwise, assessments of runout distance were performed on 'after' scans, and XY translation errors would not affect straight-line distances on individual scans of the alluvial plain.

Outer bend profile inundation error

Error measured to account for variability in profile segment size and interaction with debris-flow matter (with at most two extra segments) likely does not detract from the insights gathered in this study. The error could have been lessened by reducing segment sizes, highlighting the general and imprecise nature in which these measurements were taken from a quantitative standpoint. Otherwise, visual representations created in ArcGIS for outer bend

profile inundation were created using far more precise methods, where areas of overlap were not determined on a per-segment basis but rather from vectors outlining the boundaries of each flow. These visual representations paint a much clearer picture of overlap with runout inundation zones on the outflow plain and oppose the extreme (~5 – 10 cm) values of error suggested by the error calculations.

Order error

The unanimous agreement of low likelihood of positive relationships between the sin(1.5x) and sin(2x) groups suggests order error likely did not play a role in the experiment. This deduction helps provide legitimacy for the experimental methodology in terms of its consistency.

Nonmeasured/hypothesized sources of error

Hypothesized sources of error include channel bend placement, depths of reburial, length of the channel before peak curvature angles, orientation of printed channels during imprinting in the alluvial plain, and ability to accurately level the outflow plain between each run. Misplacement of the 3D printed channels before each trial may result in runout originating or trending laterally following avulsion. This could lead to inconsistencies in avulsion and depositional locations throughout the experiment. Inconsistencies in depths of reburial may introduce larger or smaller catchment areas within the channel, influencing the volumes of debris flows able to exit the channel. Inconsistencies in channel length leading up to peak channel curvature angle may introduce differing capacities for capturing debris-flow masses before

points of avulsion. The orientations that each printed channel was imprinted into the alluvial plain likely attributed some tangible yet currently unknown level of error on the debris-flow runout behaviors. It is unlikely that a debris-flow traveling down a steep channel will encounter a meandering channel whose sine curvature climbs back upslope, such as what would happen if the sin(1.5x) and sin(2x) curves had not been trimmed. Inaccuracies in outflow plain leveling introduce several possible issues to the experiment. These may include inconsistencies during debris-flow runout volumetric analysis, may introduce restrictions (or lack thereof) for debris-flow runout such as hypothesized with reburial depth inconsistencies, and may introduce elevation error when assessing consistency in outflow plain boundary coordinate location.

CONCLUSIONS

The goals of this experiment were to assess whether debris-flow avulsions can be modeled in clear channels, determine hotspots in zones of avulsion and runout inundation, and assess relationships between channel sinuosity and resulting avulsion and runout behaviors. The intention was to better arm communities with the knowledge necessary to better mitigate and respond to debris-flow related phenomena on alluvial fans.

Established geomorphological literature tends to repeat traditional thinking that debris-flow avulsions from meandering channels require obstruction to flow, which can be a fatal assumption when evaluating hazard risk on alluvial fans. To answer the first research question of this study, the results presented support the alternative idea that debris-flow avulsions can be initiated in channels free of debris pileup. In addition, debris-flow avulsions in our simulated environment were solely observed to be directly caused by flow superelevation in channel outer bends.

In response to the second research question of this study, zones of likely outer bend profile inundation (avulsion range) and alluvial plain inundation from runout were observed, illustrated in ArcGIS, and analyzed using more quantitative methods. It appears these variables may be spatially related on a per-channel basis judging from the ArcGIS product, though the quantitative analysis suggests a different story: variability in locations where avulsions initiate may not correspond to variation in debris-flow volumes and maximum runout between the sin(1.5x) and sin(2x) curves.

In response to the third research question of this study, additional insights were obtained using quantitative methods. The findings of the study suggest that 1) channel sinuosity has an

impact on debris-flow avulsions, with narrower curves leading to larger volumes and greater surface coverage of debris-flow runout compared to wider curves during avulsions; and 2) the volumes and maximum distances of debris-flow runout following avulsion on a single curve are probably related, but not necessarily connected to the volumes and maximum runout distances experienced after avulsion on curves with varying sine curvatures.

Limitations in this study included inconsistencies in the experimental methodology and the lack of data derived from the first two channels (sin(0.5x) and sin(1x)). Inconsistencies including displacement in channel location and variability in channel reburial depth after each trial run may have produced debris-flow behaviors unlikely to occur on natural alluvial fans. The lack of data derived from the first two channels hindered the ability to produce rating curves and potentially highlight more significant trends within the data.

The results presented may provide key insights into the behaviors of debris-flow runout on natural alluvial fans. These insights would be most appropriate for hazard mitigation, such as with the more efficient installation of debris flow barriers on alluvial fans. It is important to consider the widest range of scenarios applicable to debris-flow inundation on alluvial fans, and the use of this physical model added a few more possibilities to the playing field.

REFERENCES

Adams, K., 2017, Autogenic controls on debris-flow fans with limited accommodation space: laboratory experiments informed by a field example: East Carolina University (ECU) [thesis].

Allen, J., 2008, Alluvial Fan in Southern Iran: Zagros Mountains, southern Iran, NASA, https://earthobservatory.nasa.gov/images/36041/alluvial-fan-in-southern-iran (accessed October 2021).

Andries, P., Fasseur, C., Debie, J., Goossens, R. and Devriendt, D., 2005, Digital Close-Range Photogrammetry of Statue-Colonnes Applied on The Tournai Cathedral (Belgium), CIPA XX, Torino, Italy, v. 1, p. 82-85.

Bahrami, S., and Ghahraman, K., 2019, Geomorphological controls on soil fertility of semi-arid alluvial fans: A case study of the Joghatay Mountains, Northeast Iran: CATENA, v. 176, p. 145–158, doi: 10.1016/j.catena.2019.01.016.

Boyer, P., Roberts, N., and Baird, D., 2006, Holocene environment and settlement on the çarşamba alluvial fan, south-central Turkey: Integrating geoarchaeology and archaeological field survey: Geoarchaeology, v. 21, p. 675–698, doi: 10.1002/gea.20133.

Bull, W.B., 1977, The alluvial-fan environment: Progress in Physical Geography: Earth and Environment, v. 1, p. 222–270, doi: 10.1177/030913337700100202.

Burroughs, E.R, 1984, Landslide hazard rating for portions of the Oregon Coast Range: In Symposium on Effects of Forest Land Use on Erosion and Slope Stability. Environment and Policy Institute, East-West Center, University of Hawaii, Honolulu, HI., p. 265-274.

Cavalli, M., and Marchi, L., 2008, Characterisation of the surface morphology of an alpine alluvial fan using airborne LiDAR. Natural Hazards and Earth System Science, v. 8(2), 323-333.

Cooper, H.M., Wasklewicz, T., Zhu, Z., Lewis, W., LeCompte, K., Heffentrager, M., Smaby, R., Brady, J., and Howard, R., 2021, Evaluating the ability of multi-sensor techniques to capture topographic complexity: Sensors, v. 21, p. 2105, doi: 10.3390/s21062105.

Davies, T. R. H., 1990, DEBRIS-FLOW SURGES — EXPERIMENTAL SIMULATION: Journal of Hydrology (New Zealand), v. 29(1), p. 18–46. http://www.jstor.org/stable/43944650.

Davies, T. R. H., and McSaveney, M. J., 2008, Principles of sustainable development on fans: Journal of Hydrology (New Zealand), v. 47(1), p. 43–65. http://www.jstor.org/stable/43944963

de Haas, T., 2016, Life, death and revival of debris-flow fans on Earth and Mars (Doctoral dissertation). Utrecht University, the Netherlands.

de Haas, T., van den Berg, W., Braat, L., and Kleinhans, M.G., 2016, Autogenic avulsion, channelization and backfilling dynamics of debris-flow fans: Sedimentology, v. 63, p. 1596–1619, doi: 10.1111/sed.12275.

de Haas, T., Densmore, A., Stoffel, M., Suwa, H., Imaizumi, F., Ballesteros-Cánovas, J., and Wasklewicz, T., 2018, Avulsions and the spatio-temporal evolution of debris-flow fans: Earth-Science Reviews, v. 177, p. 53–75, doi: 10.1016/j.earscirev.2017.11.007.

De Haas, T., Densmore, A.L., den Hond, T. and Cox, N.J., 2019, Fan-surface evidence for debris-flow avulsion controls and probabilities, Saline Valley, California. Journal of geophysical research: earth surface, 124(5), pp.1118-1138.

Densmore, A. L., de Haas, T., McArdell, B. W., & Schuerch, P., 2019, Making sense of avulsions on debris-flow fans: Association of Environmental and Engineering Geologists; special publication 28. Colorado School of Mines. Arthur Lakes Library.

Ellett, N.G., Pierce, J.L., and Glenn, N.F., 2019, Partitioned by process: Measuring post-fire debris-flow and Rill erosion with structure from motion photogrammetry: Earth Surface Processes and Landforms, v. 44, p. 3128–3146, doi: 10.1002/esp.4728.

Florsheim, J.L., and Chin, A., 2021, Geomorphic responses to wildfire in fluvial systems: Reference Module in Earth Systems and Environmental Sciences, doi: 10.1016/b978-0-12-818234-5.00045-6.

Gabet, E.J., 2003, Post-fire thin debris flows: Sediment transport and numerical modelling: Earth Surface Processes and Landforms, v. 28, p. 1341–1348, doi: 10.1002/esp.590.

Galgaro, A., Tecca, P.R., Genevois, R., and Deganutti, A.M., 2005, Acoustic module of the Acquabona (Italy) debris flow monitoring system: Natural Hazards and Earth System Sciences, v. 5, p. 211–215, doi: 10.5194/nhess-5-211-2005.

Griffiths, P.G., 2004, Frequency and initiation of debris flows in Grand Canyon, Arizona: Journal of Geophysical Research, v. 109, doi: 10.1029/2003jf000077.

Hooke, R. L., 1967, Processes on arid-region alluvial fans: The Journal of Geology, v. 75, p. 438-460.

Huang, J., Li, X., Zhang, L., Li, Y., and Wang, P., 2020, Risk perception and management of debris flow hazards in the Upper Salween Valley region: Implications for disaster risk reduction in marginalized mountain communities: International Journal of Disaster Risk Reduction, v. 51, p. 101856, doi: 10.1016/j.ijdrr.2020.101856.

Huang, X., and Tang, C., 2014, Formation and activation of catastrophic debris flows in Baishui River basin, Sichuan Province, China: Landslides, v. 11, p. 955–967, doi: 10.1007/s10346-014-0465-1.

Iverson, R.M., 1997, The Physics of Debris Flows: Reviews of Geophysics, v. 35, p. 245–296, doi: 10.1029/97rg00426.

Iverson, R.M., Logan, M., LaHusen, R.G., and Berti, M., 2010, The perfect debris flow? aggregated results from 28 large-scale experiments: Journal of Geophysical Research, v. 115, doi: 10.1029/2009jf001514.

Kean, J.W., McCoy, S.W., Tucker, G.E., Staley, D.M., and Coe, J.A., 2013, Runoff-generated debris flows: Observations and modeling of surge initiation, magnitude, and frequency: Journal of Geophysical Research: Earth Surface, v. 118, p. 2190–2207, doi: 10.1002/jgrf.20148.

Kean, J.W., Staley, D.M., Lancaster, J.T., Rengers, F.K., Swanson, B.J., Coe, J.A., Hernandez, J.L., Sigman, A.J., Allstadt, K.E., and Lindsay, D.N., 2019, Inundation, flow dynamics, and damage in the 9 January 2018 Montecito Debris-flow event, California, USA: Opportunities and challenges for post-wildfire risk assessment: Geosphere, v. 15, p. 1140–1163, doi: 10.1130/ges02048.1.

Langbein, W.B., and Leopold, L.B., 1966, River meanders - theory of minimum variance: GEOLOGICAL SURVEY PROFESSIONAL PAPER 422-H, doi: 10.3133/pp422h.

Leeder, M.R., 1973, Fluviatile fining-upwards cycles and the magnitude of palaeochannels: Geological Magazine, v. 110, p. 265–276, doi: 10.1017/s0016756800036098.

Leenman, A., and Eaton, B., 2021, Mechanisms for avulsion on alluvial fans: Insights from high-frequency topographic data: Earth Surface Processes and Landforms, doi: 10.1002/esp.5059.

LibreTexts, 2020, 8.1: Arc Length, https://math.libretexts.org/Bookshelves/Calculus/Map%3A_Calculus__Early_Transcendentals_(Stewart)/08%3A_Further_Applications_of_Integration/8.01%3A_Arc_Length (accessed December 2021).

Mardhiah, U., Caruso, T., Gurnell, A., and Rillig, M.C., 2016, Arbuscular mycorrhizal fungal hyphae reduce soil erosion by surface water flow in a greenhouse experiment: Applied Soil Ecology, v. 99, p. 137–140, doi: 10.1016/j.apsoil.2015.11.027.

Martin, Y.E., 2007, Wildfire disturbance and shallow landsliding in coastal British Columbia over Millennial Time Scales: A numerical modelling study: CATENA, v. 69, p. 206–219, doi: 10.1016/j.catena.2006.05.006.

McSaveney, M.J., Beetham, R.D., and Leonard, G.S, 2005, The 18 May 2005 debris flow disaster at Matata: Causes and mitigation suggestions: Client Report 2005/71, Institute of Geological & Nuclear Sciences Ltd, p. 59.

Montgomery, D.R., and Buffington, J.M., 1998, Channel processes, classification, and response, In: Naiman R., and Bilby, R.E., River Ecology and Management: Lessons from the Pacific Ecoregion: Springer-Verlag, p. 13–41.

Nichols, G., 1991, Rachocki, A.H., and Church, M. (Eds), 1990, Alluvial Fans: A Field Approach: Geological Magazine, v. 128, p. 91–91, doi: 10.1017/S0016756800018240.

Nieto, N., Chamorro, A., Echaveguren, T., and Escauriaza, C., 2022, Fragility curves for road embankments exposed to adjacent debris flow: Progress in Physical Geography: Earth and Environment, v. 47, p. 105–122, doi: 10.1177/03091333221111444.

Okano, K., Suwa, H., and Kanno, T., 2012, Characterization of debris flows by rainstorm condition at a torrent on the Mount Yakedake Volcano, Japan: Geomorphology 136 (1), 88–94.

Over, J.-S.R., Ritchie, A.C., Kranenburg, C.J., Brown, J.A., Buscombe, D.D., Noble, T., Sherwood, C.R., Warrick, J.A., and Wernette, P.A., 2021, Processing coastal imagery with Agisoft metashape professional edition, version 1.6—structure from Motion Workflow Documentation: Open-File Report, doi: 10.3133/ofr20211039.

Paola, C., Straub, K., Mohrig, D., & Reinhardt, L., 2009, The “unreasonable effectiveness” of stratigraphic and geomorphic experiments. Earth-Science Reviews, v. 97(1), p. 1-43.

Parise, M., and Cannon, S.H., 2011, Wildfire impacts on the processes that generate debris flows in burned watersheds: Natural Hazards, v. 61, p. 217–227, doi: 10.1007/s11069-011-9769-9.

Prancevic, J.P., Lamb, M.P., and Fuller, B.M., 2014, Incipient sediment motion across the river to debris-flow transition: Geology, v. 42, p. 191–194, doi: 10.1130/g34927.1.

Procter, C.M., 2012, Debris flow dynamics: A flume study of velocity and superelevation, Durham theses, Durham University. Available at Durham E-Theses Online: http://etheses.dur.ac.uk/3587/.

Santi, P.M., Pyles, D.R., and Pederson, C.A., 2017, Debris flow avulsion: International Journal of Erosion Control Engineering, v. 10, p. 67–73, doi: 10.13101/ijece.10.67.

Scheidl, C., McArdell, B.W., and Rickenmann, D., 2014, Debris-flow velocities and superelevation in a curved laboratory channel. Canadian Geotechnical Journal, 52(3), pp.305-317.

Schumm, S.A., 1972, Fluvial palaeochannels. In Rigby, J. K. & Hamblin, W. K. (Eds): Recognition of ancient sedimentary environments. 98-107. Soc. Econ. Palaeontologists Mineralogists, Spec. Publ. 13.

Schumm, S.A., Mosley, M., Weaver, W., 1987, Experimental Fluvial Geomorphology. John Wiley and Sons, New York.

Skaggs, R.W., and de Ridder, N.A., 1996, Groundwater Investigations, in Ritzema, H.P. ed., Drainage principles and applications, Wageningen, Netherlands, International Institute for Land Reclamation and Improvement, p. 1125.

Suwa, H., Okano, K., Kanno, T., 2009, Behavior of debris flows monitored on test slopes of Kamikamihorizawa Creek, Mount Yakedake, Japan. Int. J. Erosion Control Eng. 2 (2), 33–45.

Suwa, H., Okunishi, K., and Sakai, M., 1993, Motion, debris size and scale of debris flows in a valley on Mount Yakedake, Japan, IAHS Publ. No. 217: 239-248.

Takahashi, T., 2009, A review of Japanese Debris Flow Research: International Journal of Erosion Control Engineering, v. 2, p. 1–14, doi: 10.13101/ijece.2.1.

Turnbull, B., Bowman, E.T., and McElwaine, J.N., 2015, Debris flows: Experiments and modelling: Comptes Rendus Physique, v. 16, p. 86–96, doi: 10.1016/j.crhy.2014.11.006.

Wang, Z., You, Y., Zhang, G., Feng, T., Liu, J., Lv, X., and Wang, D., 2020, Superelevation analysis of the debris flow curve in Xiedi Gully, China: Bulletin of Engineering Geology and the Environment, v. 80, p. 967–978, doi: 10.1007/s10064-020-01999-1.

Wheaton, J.M., Brasington, J., Darby, S.E., and Sear, D.A., 2009, Accounting for uncertainty in DEMS from repeat topographic surveys: Improved sediment budgets: Earth Surface Processes and Landforms, doi: 10.1002/esp.1886.

Whipple, K.X., and Dunne, T., 1992, The influence of debris-flow rheology on fan morphology, Owens Valley, California: Geological Society of America Bulletin, v. 104, p. 887–900, doi: 10.1130/0016-7606(1992)104<0887:tiodfr>2.3.co;2.

Williams, G.P., 1986, River meanders and channel size: Journal of Hydrology, v. 88, p. 147–164, doi: 10.1016/0022-1694(86)90202-7.

Zubrycky, S., Mitchell, A., McDougall, S., Strouth, A., Clague, J.J., and Menounos, B., 2021, Exploring new methods to analyse spatial impact distributions on debris-flow fans using data from south-western British Columbia: Earth Surface Processes and Landforms, v. 46, p. 2395–2413, doi: 10.1002/esp.5184.